THE ASTROPHYSICAL JOURNAL, 416:623–646, 1993 October 20

ROSAT X-RAY STUDY OF THE CHAMAELEON I DARK CLOUD. I. THE STELLAR POPULATION

ERIC D. FEIGELSON,[1] SOPHIE CASANOVA,[2] THIERRY MONTMERLE,[2] AND JEAN GUIBERT[3]

Received 1992 December 21; accepted 1993 April 28

ABSTRACT

Two soft X-ray images of the Chamaeleon I star-forming cloud obtained with the *ROSAT* Position Sensitive Proportional Counter are presented. Seventy reliable, and 19 possible additional, X-ray sources are found. Eighty percent of these sources are certainly or probably identified with T Tauri stars formed in the cloud. Nineteen to 39 are proposed new "weak" T Tauri (WTT) stars which, when confirmed by optical spectroscopy, will significantly enlarge the known cloud population. Individual T Tauri X-ray luminosities range from $\sim 6 \times 10^{28}$ to $\sim 2 \times 10^{31}$ ergs s^{-1} (0.4–2.5 keV), or $\sim 10^2$–10^4 times solar levels. The *ROSAT* images are an order of magnitude more sensitive, with 3–4 times more stellar identifications, than earlier *Einstein Observatory* images of the cloud.

A wide range of issues is addressed by these data. The spatial distribution and Hertzsprung-Russell diagram locations of the stars indicate that WTT stars and "classical" T Tauri (CTT) stars are coeval. Their X-ray luminosity functions are also essentially identical, suggesting that CTT stars have the same surface magnetic activity as WTT stars. The X-ray luminosities of well-studied Chamaeleon I cloud members are strongly correlated with a complex of four stellar properties: bolometric luminosity, mass, radius, and effective temperature. The first relation can be expressed by the simple statement that low-mass Chamaeleon I stars have $L_X/L_* = 1.6 \times 10^{-4}$, within a factor of ± 2 ($1\ \sigma$) and the radius relation by $F_X \propto R_*$. There is thus no evidence of magnetic saturation of the stellar surfaces. We find no evidence for the absorption of soft X-rays in CTT winds and/or boundary layers traced by the strength of the Hα emission. The mean X-ray luminosity for an unbiased optically selected T Tauri sample is 1.6×10^{29} ergs s^{-1}, and we find evidence for temporal evolution of X-ray emission for stars within the pre–main-sequence evolutionary phase. The total pre–main-sequence population ($M_* > 0.1\ M_\odot$) of the cloud is estimated to be $\gtrsim 200$ stars, with X-ray–detected WTT stars outnumbering X-ray–detected CTT stars by at least 2:1. The inferred star formation efficiency for the cloud cores is $\approx 20\%$.

Subject headings: ISM: individual (Chamaeleon I) — stars: activity — stars: pre–main-sequence — X-rays: stars

1. INTRODUCTION

One of the principal impacts of the first decade of imaging X-ray astronomy on stellar astrophysics was the demonstration that low-mass stars have their most active X-ray emission during the pre–main-sequence phase of evolution. Dozens of these stars appeared at levels $\sim 10^2$–10^4 typical main-sequence levels in *Einstein Observatory* images of nearby star-forming clouds such as Orion (Ku, Righini-Cohen, & Simon 1982; Caillault & Zoonematkermani 1989; Strom et al. 1990), Ophiuchus (Montmerle et al. 1983), Taurus-Auriga (Feigelson et al. 1987; Walter et al. 1988), and Chamaeleon I (Feigelson & Kriss 1989, hereafter FK89).

Many of the X-ray–emitting pre–main-sequence stars were unknown prior to X-ray study. These newly discovered stars were found to lack many of the traditional signposts of classical T Tauri stars, such as broad optical emission lines and photometric excesses in the ultraviolet and infrared bands. These stars were dubbed the "weak-lined" or "weak" T Tauri (WTT) stars, as opposed to the "classical" T Tauri (CTT) stars, and appear to dominate the low-mass pre–main-sequence population. There is now a widespread consensus that the main difference between the two stellar types is that CTT stars have a massive circumstellar accretion disk interacting with the young star. Their strong emission lines are probably produced either in the disk-star boundary layer and/or a wind (see review by Bertout 1989).

The X-ray characteristics of CTT and WTT stars, including spectra, strong variability, and occasional flares up to $\sim 10^{32}$ ergs s^{-1}, point to greatly enhanced solar-type magnetic activity. This interpretation is supported by optical evidence for cool starspots covering 5%–40% of the surfaces, enhanced optical/UV chromospheric emission, and (at least in the case of WTT stars) powerful nonthermal radio flares. The web of multiwavelength evidence for enhanced magnetic activity in WTT and CTT stars is detailed in recent reviews by Bertout (1989), Feigelson, Giampapa, & Vrba (1991), and Montmerle et al. (1993).

While *Einstein* images provided our basic knowledge of enhanced keV X-ray emission in young stars, they have many limitations: their low sensitivity restricts detections of X-ray luminosities $\gtrsim 10^{29}$ ergs s^{-1}; poor spatial resolution around $\pm 1'$ produces a high fraction of ambiguous stellar identifications in crowded star-forming regions; poor spectral resolution combined with differing obscuration toward different stars gives only primitive information on the X-ray spectra and

[1] Department of Astronomy & Astrophysics, Pennsylvania State University, University Park, PA 16802. E-mail: edf@astro.psu.edu (Internet).
[2] Service d'Astrophysique, Centre d'Études de Saclay, 91191 Gif-sur-Yvette Cedex, France. E-mail: casa@atlantis.saclay.cea.fr,montmerle@sapvxg.saclay.cea.fr (Internet).
[3] Observatoire de Paris and Centre d'Analyse des Images, 61 Avenue de l'Observatoire, F-75014, Paris, France. E-mail: guibert@frmeu51.bitnet.

astrophysical origin. Many of these problems are alleviated with the Position Sensitive Proportional Counter (PSPC) on board *ROSAT*, the Röntgen Satellite (Trümper 1990). The X-ray images reported here using this instrument show an order-of-magnitude improvement in sensitivity and error circle areas compared to the *Einstein* data presented by FK89.

The Chamaeleon I cloud is excellent for X-ray study of CTT and WTT stars: it is more compact (about 1° × 2°) than the Taurus-Auriga complex, and closer (around 140 pc) than the Orion complex. It is quite comparable to the ρ Ophiuchi cloud in size and distance. Although relatively small, it is rich with young stars. Optical studies show about 65 unobscured cloud members about equally divided between CTT and WTT stars, four Herbig-Haro objects, four reflection nebulae, and about 25 embedded stars found in infrared surveys (Schwartz 1977; Whittet, Prusti, & Wesselius 1991; Prusti, Whittet, & Wesselius 1992, hereafter P92; Gauvin & Strom 1992, hereafter GS92; Schwartz 1992, hereafter S92). FK89 detected 21 X-ray–emitting stars in three short, overlapping exposures with the *Einstein* Imaging Proportional Counter, at least four of which are previously unidentified WTT stars (FK89; Walter 1992, hereafter W92).

One difficulty concerning the Chamaeleon I cloud has been uncertainty in its distance, with published estimates ranging from 115 to 220 pc. However, recent research has led to a growing consensus on a distance around 140 pc (S92). The spectral energy distributions and extinction models for the B9/B9.5 cloud members HD 97300 and HD 97048 have been reanalyzed (Steenman & Thé 1989; S92; Davies et al. 1991), giving $d \simeq 140$–150 pc. Whittet et al. (1987) obtained 140 pc from color excess versus distance measurement for field stars projected on the cloud, although this estimate depends on only four stars that are not accurately characterized (GS92). However, a sudden increase in absorption at $d \simeq 137$ pc has been confirmed by Franco (1991) for a much larger sample of field stars in a region several degrees in extent north and east of the Cha I cloud. Consequently we adopt here a distance $d = 140$ pc, adjusting published stellar properties (e.g., in GS92, who take $d = 215$ pc) to this distance.

The present study (Paper I) first presents the astronomical data: the location of 89 X-ray sources found in two overlapping *ROSAT* PSPC fields, finding charts, and suggested optical-infrared stellar identifications (§§ 2–3). We then investigate the global and statistical properties of the X-ray–emitting stellar population including the spatial and luminosity distribution (§§ 4–5), evolution of X-ray emission (§ 6), relationships between X-ray and optical-infrared properties (§ 7), estimates of the total cloud stellar population, and star formation history of the cloud (§ 8). We emphasize questions raised, but not fully answered, in *Einstein*-era studies. Is WTT and CTT activity magnetic in origin and induced by a dynamo mechanism? Are X-rays absorbed in CTT circumstellar components, or can circumstellar material contribute to the X-ray emission? What are the evolutionary relationships and relative population sizes of CTT and WTT stars? Do pre–main-sequence stars follow well-established activity-rotation-age relationships found in older stars? A later study (Casanova et al. 1993, Paper II) will use a larger data set and will emphasize the astrophysics of the X-ray emission including spectral and variability analysis of individual sources.

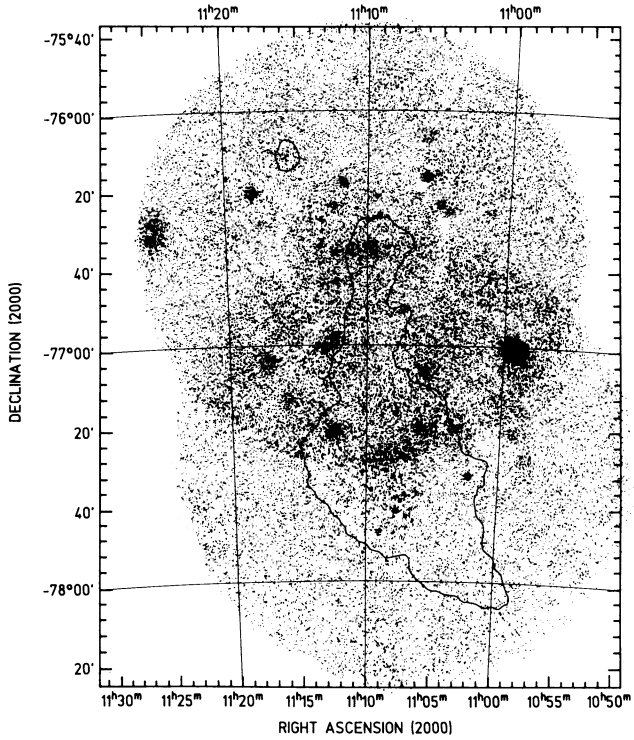

FIG. 1.—Mosaic of the two Chamaeleon *ROSAT* fields, with each photon in the PSPC 0.4–2.5 keV band indicated by a black dot. The contours indicate intensity of *IRAS* 100 μm emission, outlining the large-scale shape of the cloud.

2. X-RAY OBSERVATIONS AND ANALYSIS

2.1. *X-Ray Source Detection*

The two *ROSAT* PSPC images analyzed here, each with exposure $\simeq 6000$ s, are summarized in Table 1. These images (North and South) correspond to fields 1 and 2, respectively. Figure 1 shows a mosaic of these fields in the "hard" band (defined as the band beyond the carbon absorption edge of the PSPC window, i.e., 0.4–2.5 keV), with an outline of the underlying molecular cloud. Numerous pointlike sources are visible, which are most clearly seen in the contour maps shown in Figures 2 and 3. A third field, taken with a boron filter and overlapping our two fields, is being used for a study of spatial variations in the diffuse X-ray emission (due to shadowing by

TABLE 1

LOG OF *ROSAT* OBSERVATIONS

FIELD	FIELD CENTER (J2000)		OBSERVING TIMES				EXPOSURE (s)
			Day (1991)	UT	Day (1991)	UT	
1.....	$11^h10^m33^s6$	−76°36′00″	9 Feb	22:14:47 to	18 Feb	17:59:12	6265
2.....	11 07 24.0	−77 31 12	6 Mar	09:12:19 to	6 Mar	13:05:13	5662

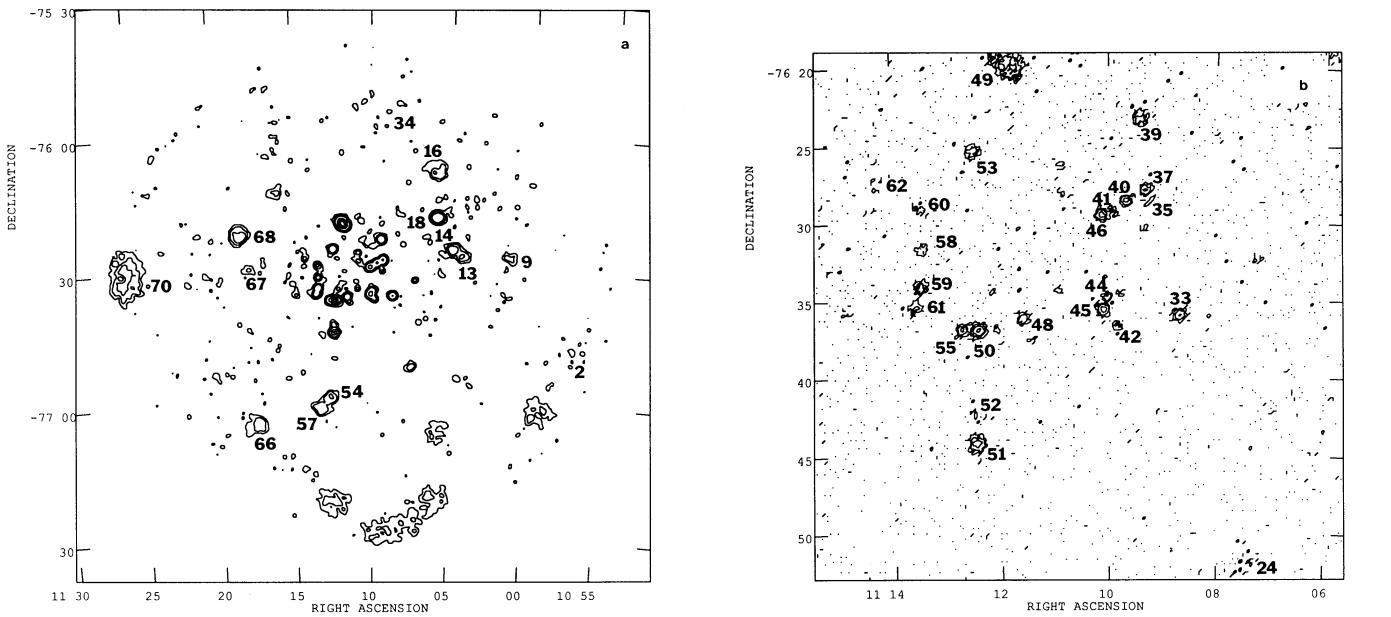

FIG. 2.—Contour maps of field 1, the northern portion of the Chamaeleon I cloud, in the *ROSAT* PSPC 0.4–2.5 keV band. (*a*) The entire field, smoothed with a 1′ FWHM Gaussian. The lowest contours are 1.5%, 3%, and 6% of the peak. (*b*) The inner region, unsmoothed with 20″ pixel^{-1}. The contours represent 1, 3, 9, and 27 photons pixel^{-1}. Background has not been removed from either image. Sources from Table 2 are numbered.

the cloud; Mendenhall & Burrows 1993). This field has kindly been made available to us to provide better source localization in the central parts of the cloud.

The detection of X-ray sources is based on the analysis in the pipeline processing, *ROSAT* Standard Analysis Software System (SASS) version 5.2. This is a complex process wherein each field is examined in three energy bands, tentative sources are located by an excess of photons above both local and global maps of the background using a maximum-likelihood criterion, and overlapping sources are merged to form a master list of distinct sources. This process located 90 sources: 48 sources in field 1 and 42 sources in field 2. We found the SASS lists had to be modified in various ways. First, coincident sources found in both fields were merged, and sources blurred at the edge of one field were deleted when they were well-resolved in the center of the other field. Second, visual inspection of the images and contour maps located several sources missed by the SASS algorithms, when the sources were close to a nearby strong source (CHXR 13, 19, 35, 41, 54, 55, and 57), and two cases where weak sources were missed (CHXR 63, 86). The result is a final list of 89 distinct X-ray sources listed (in order of increasing right ascension) in

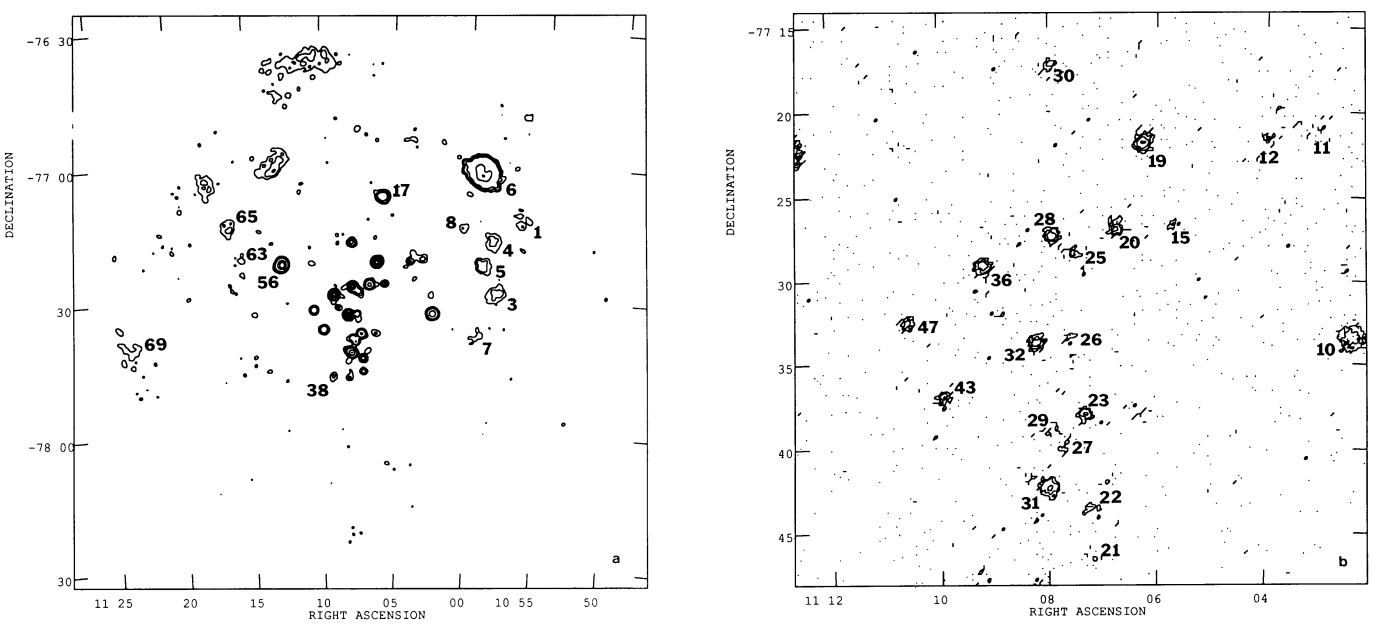

FIG. 3.—Contour maps of field 2, the southern portion of the cloud. All parameters are identical to those in Fig. 2.

TABLE 2

ROSAT X-RAY SOURCES IN THE CHAMAELEON I CLOUD

CHXR	Field	α (J2000) h m s	δ ° ′ ″	± ″	θ ′	Count rate Cts/ks	±	S/N	Einstein Src. CHX	Sep(″)	Notes
1	2	10 56 35.8	-77 11 53	30	40	8.7	1.7	5.2[d]	1	66	
2	1	10 57 02.6	-76 47 56	30	48	18.0	3.8	4.7[f]	...	...	
3	2	10 58 05.2	-77 28 51	30	30	14.6	2.1	7.1[d]	...	...	
4	2	10 58 27.2	-77 17 04	30	32	11.9	1.8	6.8[d]	2	64	
5	2	10 59 03.3	-77 22 33	30	28	13.6	1.8	7.4[d]	...	...	
6	2	10 59 10.8	-77 01 43	30	40	466.4	11.5	40.5[f]	3	16	⋆
	1	10 59 08.3	-77 01 17	30	46	41.6	4.9	8.5[f]	...	...	⋆
7	2	10 59 24.1	-77 38 27	30	27	3.7	1.1	3.5[e]	...	...	
8	2	11 00 19.7	-77 14 09	30	29	4.8	1.2	4.1[d]	...	...	
9	1	11 01 16.0	-76 27 23	30	33	10.0	1.7	5.9[b]	...	...	
10	2	11 02 25.8	-77 33 32	4	16	40.1	2.8	14.2[c]	4	30	
11	2	11 03 12.1	-77 21 05	15	17	2.6	0.8	3.5[c]	...	...	
12	2	11 03 58.6	-77 21 39	5	15	4.0	0.9	4.5[c]	...	...	
13	1	11 04 11.2	-76 27 04	30	15	9.8	1.6	6.3[c]	...	...	⋆
14	1	11 04 49.7	-76 25 32	30	23	22.1	2.2	10.1[d]	...	...	
15	2	11 05 43.7	-77 26 48	4	7	3.3	0.8	4.2[b]	...	...	
16	1	11 05 51.7	-76 08 00	30	33	30.3	3.9	7.8[f]	...	...	
17	2	11 05 51.8	-77 07 23	30	24	22.6	2.3	9.8[d]	6	15	
	1	11 05 50.4	-77 06 34	30	34	17.9	3.3	5.5[f]	...	...	
18	1	11 05 53.7	-76 18 26	30	24	29.5	2.5	11.9[d]	...	...	
19	2	11 06 16.2	-77 21 59	4	10	56.1	3.2	17.7[d]	7	15	
	1	11 05 40.1	-77 21 16	30	48	46.4	5.1	9.2[f]	...	...	⋆
20	2	11 06 45.7	-77 27 00	4	5	19.3	1.9	10.4[c]	8	33	
21	2	11 07 11.8	-77 46 40	8	15	3.1	0.8	3.7[c]	...	...	
22	2	11 07 13.4	-77 43 47	4	13	5.4	1.0	5.2[c]	...	...	
23	2	11 07 20.7	-77 38 07	4	7	15.4	1.7	9.1[b]	9	16	
24	1	11 07 28.5	-76 51 57	12	19	6.2	1.7	3.7[e]	...	...	
25	2	11 07 33.1	-77 28 30	4	3	6.9	1.1	6.0[c]	...	...	
26	2	11 07 37.8	-77 33 35	5	3	2.7	0.7	3.8[b]	...	...	
27	2	11 07 48.4	-77 39 33	15	8	3.2	0.8	4.1[b]	...	...	
28	2	11 07 56.6	-77 27 27	4	4	33.1	2.4	13.6[c]	10	45	
29	2	11 07 58.0	-77 39 03	17	8	2.9	0.7	3.9[b]	...	...	
30	2	11 07 59.2	-77 17 29	8	14	5.5	1.0	5.3[c]	...	...	
31	2	11 08 00.6	-77 42 27	4	11	33.1	2.5	13.2[c]	11	26	
32	2	11 08 14.4	-77 33 53	4	4	29.3	2.3	12.7[b]	12	30	
33	1	11 08 40.5	-76 36 06	4	6	11.2	1.3	8.3[a]	13	42	
34	1	11 08 57.3	-75 53 51	30	43	14.6	3.4	4.3[f]	...	...	
35	1	11 09 10.6	-76 28 40	30	9	2.1	0.6	3.6[b]	...	...	⋆
36	2	11 09 12.6	-77 29 15	4	6	37.8	2.7	14.1[c]	14	19	
37	1	11 09 17.9	-76 27 59	4	9	12.9	1.4	9.2[b]	...	...	
38	2	11 09 20.0	-77 47 46	15	18	3.4	0.9	3.7[c]	...	...	
39	1	11 09 24.5	-76 23 24	4	13	13.5	1.5	8.8[b]	...	...	
40	1	11 09 39.8	-76 28 39	4	8	13.6	1.5	9.2[b]	...	...	
41	1	11 09 52.7	-76 29 21	20	7	2.1	0.6	3.8[a]	15	21	⋆
42	1	11 09 49.6	-76 36 51	4	3	3.1	0.7	4.5[a]	...	...	
43	2	11 09 57.3	-77 37 08	4	10	10.0	1.4	7.4[b]	17	36	
44	1	11 10 01.7	-76 34 56	4	2	7.5	1.1	6.6[a]	...	...	
45	1	11 10 05.3	-76 35 45	4	2	14.8	1.5	9.6[a]	16	27	
46	1	11 10 06.8	-76 29 38	4	7	17.7	1.7	10.6[b]	...	...	
47	2	11 10 36.7	-77 32 42	4	11	9.5	1.3	7.2[b]	...	...	
48	1	11 11 34.5	-76 36 21	4	4	10.2	1.3	8.0[b]	...	...	
49	1	11 11 49.8	-76 19 48	4	17	120.6	4.6	26.0[d]	18	42	⋆
50	1	11 12 24.3	-76 37 06	4	7	48.9	2.9	17.1[b]	20	26	
51	1	11 12 27.0	-76 44 23	4	11	30.0	2.2	13.6[b]	19	8	
	2	11 12 44.5	-76 44 41	30	50	20.5	3.5	5.9[f]	...	...	
52	1	11 12 28.5	-76 42 33	7	9	2.8	0.7	3.8[c]	...	...	
53	1	11 12 28.9	-76 25 31	4	13	15.4	1.6	9.3[b]	...	...	
54	1	11 12 39.3	-76 58 48	30	24	16.3	1.9	8.4[b]	21	...	
55	1	11 12 42.2	-76 37 04	15	7	12.8	1.4	9.0[b]	...	...	⋆
56	2	11 12 43.8	-77 22 26	4	20	95.1	4.6	20.5[d]	22	25	
	1	11 12 36.4	-77 21 53	30	46	49.3	4.8	10.4[f]	...	...	
57	1	11 13 24.4	-77 01 17	30	26	13.9	1.8	7.6[b]	...	...	
58	1	11 13 26.2	-76 31 53	4	11	5.3	1.0	5.5[b]	...	...	
59	1	11 13 27.1	-76 34 17	4	10	11.2	1.3	8.3[b]	...	...	
60	1	11 13 28.0	-76 29 10	6	12	3.8	0.8	4.7[b]	...	...	

TABLE 2—*continued*

CHXR	Field	α (J2000) h m s	δ ° ′ ″	± ″	θ ′	Count rate Cts/ks	±	S/N	Einstein Src. CHX	Sep(″)	Notes
61	1	11 13 34.1	-76 35 37	4	11	6.9	1.1	6.6[b]	...	...	
62	1	11 14 16.1	-76 27 37	8	16	2.3	0.6	3.5[b]	...	...	
63	2	11 15 50.0	-77 20 48	30	30	7.8	1.8	4.3[e]	...	...	★
64	1	11 16 03.5	-76 12 50	30	30	12.1	3.0	4.1[f]	...	...	
65	2	11 16 16.9	-77 14 04	30	34	11.1	1.7	6.4[c]	...	...	
66	1	11 17 36.4	-77 04 27	30	37	33.5	4.0	8.3[f]	...	...	
	2	11 17 37.9	-77 04 50	30	43	27.3	3.9	7.1[f]	...	...	
67	1	11 17 52.4	-76 29 58	30	26	5.4	1.2	4.4[d]	...	...	
68	1	11 18 22.4	-76 22 18	30	31	34.3	2.7	12.6[d]	...	...	
69	2	11 23 23.3	-77 39 58	30	52	30.0	4.3	7.0[c]	...	...	
70	1	11 25 32.6	-76 31 07	30	53	175.1	8.0	21.9[f]	...	...	

Tables 2 and 3. The "CHXR" acronym designates a "Chamaeleon I X-ray *ROSAT*" source, distinguished from the *Einstein* "CHX" sources in FK89.

2.2. *Source Positions*

When the X-ray source with accurate SASS positions (i.e., strong sources close to the field center) were compared to the digitized optical star field (§ 3.1), small systematic offsets of X-ray sources from likely stellar identifications were clearly seen. Quantitative analysis of 21 sources with SASS positional uncertainties $<5''$ associated with isolated prominent stars showed the X-ray sources on average lay 8″ east and 6″ north in field 1, and 4″ east in field 2, of stellar locations. (Our optical astrometry is described in Appendix A.) These offsets are probably due to boresight errors in the *ROSAT* aspect solution (see MPE ROSAT Status Report, No. 10, 1992 August 1). After correction of these small offsets, X-ray and optical positions agree to within $\pm 3''$ (1 σ). This indicates superb performance of the *ROSAT* aspect and proportional counter systems.

While the X-ray positions of sources in the well-focused inner region of the detector are excellent after boresight correction, they do not appear very accurate in the outer regions.

TABLE 3

ADDITIONAL POSSIBLE X-RAY SOURCES

CHXR	Field	α (J2000) h m s	δ ° ′ ″	± ″	θ ′	Count rate Cts/ks	±	S/N	Notes
71	2	11 02 33.1	-77 29 26	9	16	1.8	0.6	2.8	
72	1	11 04 14.1	-76 54 33	30	28	6.9	2.8	2.5[f]	
73	2	11 06 26.5	-77 37 38	12	7	1.0	0.5	2.1[b]	
74	2	11 06 54.0	-77 42 09	9	11	1.7	0.6	2.8	
75	1	11 07 15.6	-76 32 29	6	12	2.3	0.9	2.7[d]	
76	2	11 07 33.9	-77 34 44	7	4	1.1	0.5	2.4	
77	2	11 08 10.4	-77 48 00	10	17	2.8	0.8	3.3	
78	2	11 08 54.2	-77 32 11	8	5	2.0	0.6	3.2	
79	1	11 09 19.7	-76 30 30	5	7	1.7	0.6	3.1[b]	
80	1	11 10 51.3	-76 28 10	7	8	1.6	0.5	3.1[b]	
81	1	11 10 52.9	-76 26 24	5	10	2.3	0.7	3.4[b]	
82	1	11 10 54.9	-76 34 33	5	2	1.2	0.5	2.7[a]	
83	1	11 11 24.9	-76 37 42	5	4	1.2	0.4	2.7[a]	
84	1	11 12 05.7	-76 37 02	6	6	1.8	0.6	3.3[a]	
85	1	11 12 08.9	-76 34 33	5	6	1.3	0.5	2.7[a]	
86	2	11 14 38.0	-77 34 05	30	24	5.4	1.8	2.9[e]	★
87	1	11 14 50.9	-76 35 45	9	15	1.8	0.7	2.8[c]	
88	1	11 16 21.3	-76 04 23	30	38	8.3	2.6	3.2[f]	
89	1	11 16 56.9	-75 50 22	30	51	10.0	3.7	2.7[f]	

NOTES TO TABLES 2 AND 3:

All sources with off-axis distance $\theta > 20'$: The 90% error circle radius is formally stated to be 30″, but may in some cases be larger (see text). S/N is measured in the following radii about the source centroid: $a = 20''$, $b = 35''$, $c = 50''$, $d = 100''$, $e = 150''$, and $f = 300''$.

6: This source has its count rate multiplied by more than 10 between fields 1 and 2, indicating a strong flare activity (see Paper II). In this paper we consider only the "normal" count rates of field 1, close to the average values seen in other *ROSAT* orbits.

9, 24: Sources 1′–2′ from a PSPC window support structure ("rib"). The true count rate may be somewhat higher than listed.

13, 19, 35, 41, 54, 55, 57: Source not listed in SASS Master Source List, due to proximity to a stronger nearby source. Count rate given is for hard band in the circular region of the radius given in the S/N column.

49: Extended structure. May be deconvolved into a NE component at $11^h11^m50^s$–76°19′.3 and a SW component at $11^h11^m45^s$–76°19′.8.

63, 86: Source not listed in SASS Master Source List, due to low count rate. Count rate given is for hard band in the circular region of the radius given in the S/N column.

This can be seen in sources which appear in both fields 1 and 2 (CHXR 6, 17, 51, 56, and 66), where the X-ray positions are offset by 20″–60″. Large offsets are seen even for high signal-to-noise (S/N) sources like CHXR 6, where the SASS maximum-likelihood estimate of the error is only a few arcseconds. Examination of 20 sources in common between the boron filter field and our fields give similar results: positional agreement within 10″ for sources with $\theta < 20'$ of the detector axes and have small SASS errors, but discrepancies up to 80″ if the sources lie 20′–40′ from the detector axes. This is probably due in part to the fact that the point-spread function deviates strongly from a Gaussian far from the axis, even becoming hollow toward the edge of the field, as can be seen on CHXR 6 and 70. The current version of the SASS software does not account for these unusual off-axis point-spread functions.

From this analysis, we have adopted the following estimated 90% error radii, which are generally more conservative than those calculated by the SASS maximum-likelihood algorithms: for $\theta < 20'$ we adopt the SASS errors unless it falls below $\pm 4''$, our estimate of the remaining systematic boresight and astrometry uncertainties; and for $\theta > 20'$, we estimate positional uncertainty of at least $\pm 30''$. We also suspect, based on possible optical identifications (see Appendix B, sources 71–89), that the SASS error radii for weak (S/N < 3.5) sources are too small, but we do not have quantitative data to make an improved error analysis.

2.3. *X-Ray Luminosities*

The statistical significances of the sources are difficult to evaluate from the pipeline process, since it combines the results of several nonlinear calculations. We therefore reevaluated the statistical significance of each source using a simple procedure. Restricting the analysis to the "hard" band (0.4–2.5 keV), which contains most of the source counts and omits most of the non–X-ray background counts, we assumed each field has a constant level of background estimated from a large source-free region. These background levels are 1.30 ± 0.09 and 0.75 ± 0.06 counts arcmin^{-2} for fields 1 and 2, respectively.[4] Subtracting these background levels, the counts in circles of various radii were measured around each source until the S/N ratio was maximized. Count rates were then obtained by dividing the counts by the vignetting-corrected exposure. From subjective examination of the images, we suspect that some of these sources with $2.4 < \mathrm{S/N} < 3.5$ do not truly exist. These marginal sources are placed in Table 3 to segregate them from the stronger reliable sources.

For scientific analyses requiring estimates of intrinsic X-ray strength, we provide two estimates of soft X-ray luminosities from the background-subtracted PSPC count rates given in Tables 2 and 3. For the sources detected in both fields, we take the count rates from the field where the source has the smaller off-axis distance, except in the case of CHXR 6 where we keep the value of field 1.[5] First, for each CHXR source we compute the *approximate* luminosity $\tilde{L}_X$ proportional to the count rates. These approximate values do not take into account individual differences in intrinsic source spectra or temporal variability. A regression between hard-band count rates and intrinsic fluxes from multiparameter spectral fitting for the strongest sources, discussed in Paper II, yields an approximate conversion from counts to fluxes: 1 count ks^{-1} = 1.3×10^{-14} ergs s^{-1} cm^{-2} in the 0.4–2.5 keV band. Individual sources show a factor of 2 scatter about this line. Assuming a cloud distance $d = 140$ pc, the conversion to $\tilde{L}_X$ is 1 count ks^{-1} = 3×10^{28} ergs s^{-1}.

Second, for 40 sources that are clearly identified with well-studied T Tauri stars having optically measured reddening, X-ray luminosities L_X corrected for foreground absorption were computed. The L_X values were obtained using the A_V values given in GS92 and a calibration curve relating X-ray flux and A_V derived from full spectral fits to five strong PSPC sources. These fits assumed the emitting region is a Raymond-Smith thermal plasma with temperature $kT = 1$ keV and solar abundances of elements. Foreground X-ray absorption is based on Morrison-McCammon atomic cross sections and assumes a conversion of $N_H/A_V = 1.9 \times 10^{21}$ cm^{-2} mag^{-1}. The conversion factor 1 count ks^{-1} = 3×10^{28} ergs s^{-1} used for $\tilde{L}_X$ values is found to correspond to $A_V \simeq 1$. The 40 values of L_X are given in Table 6 discussed below.

Analysis of samples of T Tauri stars selected independently of these *ROSAT* observations requires determination of upper limits to stars that are not detected in these fields. Detailed examination of the marginally significant sources in Table 3, and the faint but more significant sources in Table 2, shows that the detectability of sources by the SASS algorithms depends mostly on distance off-axis. We find that, considering the scatter in faint source count rates, any star with $\theta < 20'$ of the field center with >2.0 PSPC counts ks^{-1} would have been detected. This value is applied despite differences in exposure times between the two fields and due to vignetting. However, sensitivity is enormously degraded outside the inner region, far greater than expected for vignetting alone. This is because the *ROSAT* mirror point-spread function is seriously degraded for $20' < \theta < 40'$ and the SASS detection algorithm is much less efficient. For this outer region, we find a sensitivity limit of 10.0 PSPC counts ks^{-1} is valid for both fields.

The statistical analysis of these independently selected samples requires special methods because many of the stars are nondetections or "censored" data points. These methods include the maximum-likelihood Kaplan-Meier estimator of the luminosity function, and a variety of two-sample comparison tests, correlation tests, and linear regressions. These methods are discussed in detail by Schmitt (1985), Feigelson & Nelson (1985), and Isobe, Feigelson, & Nelson (1986). All calculations involving censored data are performed with revision 1.2 of the ASURV software package, which is publicly available (LaValley, Isobe, & Feigelson 1992).

2.4. *Source Lists*

Tables 2 and 3 provide the following data for the 89 sources based on the discussion above: CHXR source number (col. [1]); the field number from Table 1 (col. [2]); right ascension and declination in J2000 coordinates, after application of the field-dependent boresight corrections (cols. [3]–[4]); estimated 90% positional error radius (col. [5]); distance off-axis (col. [6]); source count rate and its error over the "hard" *ROSAT* energy band 0.4–2.5 keV, after background subtraction and correction for telescope vignetting, calculated by the SASS processing using a local background estimate (cols. [7]–[8]); the maximum S/N ratio, measured by us as described above (col. [9]); the corresponding *Einstein Observatory* X-ray source

[4] The levels differ more than expected from the exposure times, probably due to absorption of the diffuse X-ray background by the larger southern portion of the cloud (Mendenhall & Burrows 1993). Our omission of vignetting correction of the background has negligible effect.

[5] Further analysis (Paper II) shows that the approximately tenfold rise for CHXR 6 seen in field 2 is due to a short-lived flare event. The level seen in field 1 is more typical for this source.

TABLE 4

PROPOSED IDENTIFICATIONS

CHXR	Class	Reliability	Offset ″	ESO R	GSC	Cha I No.	Other Name	Near-IR	Far-IR	Notes
1	C	2	21	12.2	9414_0266	T4	SY Cha	P92	FSC	
2	?	3	...	...	...	...	...	...	...	★
3	New	2	25	11.2	...	...	...	...	...	★
4	C	2	38	...	...	T6	SZ Cha	P92	GS92	★
5	C	1	11	12.8	9414_0289	T7	TW Cha	P92	FSC	
6	C	1	13	10.5	9414_0186	T8	LkHα332-20	P92	FSC	
7	New	2	29	14.6	...	...	...	...	...	
8	New	1	33	11.0	9414_0444	...	...	...	...	★
9	New	2	22	12.2d	9410_2542	...	...	...	...	★
10	C	1	5	10.8	9914_0574	T11	CS Cha	P92	FSC	
11	New	1	1	10.5	9914_0642	...	...	...	...	
12	New	1	8	14.4	...	...	...	...	...	
13	C	1	20	...	...	T14	CT Cha	P92	FSC	★
14	New	2	9	...	...	...	...	...	...	★
15	New	1	4	16.0	...	...	...	...	...	
16	U	1	23	7.8	9410_1954	...	SAO 256798	...	...	★
17	U	1	4	12.4	9914_0032	...	...	...	...	★
18	W	1	4	12.8	9410_2619	T20	UV Cha	...	...	
19	W	1	5	...n	9414_0787	T21	Ced 110	P92	FSC	★
20	New	1	3	14.4	...	...	...	...	...	★
21	New	1	1	15.3	...	...	...	...	...	
22	New	2	2	17.2	...	...	...	...	...	★
23	C	1	1	...n	9414_0743	T26	LHα332-17	P92	FSC	★
24	C	1	15	13.8	9410_0412	T27	VV Cha	P92	FSC	
25	New	1	2	15.0	...	...	...	...	...	
26	New	1	2	17.6	...	...	...	...	...	
27	C	1	17	...n	...	T28	HM 15	P92	...	★
28	W	1	2	12.1	9414_0766	...	CHX 10a	...	...	★
29	C	2	25	...n	9414_0795	T32	HD 97048	P92	FSC	★
30	New	1	4	18.1	...	...	...	S92	FSC	★
31	C	1	4	12.0	9414_0754	T31	VW Cha	P92	...	
32	W	2	2	11.7d	9414_0640	T33	Glass I	P92	FSC	★
33	New	1	2	14.4	...	...	CHX 13a	...	...	★
34	New	2	45	...	9410_2002	...	...	...	...	★
35	New	2	...	...	...	...	...	S92	...	★
36	W	2	3	12.0d	9414_0227	T39	Sz 30	...	...	★
37	New	1	2	12.7	9410_2698	...	...	...	...	
38	U	1	9	8.3	9414_0695	...	SAO 256804	...	...	★
39	C	1	4	11.7	9410_2375	T40	VZ Cha	P92	FSC	
40	New	1	1	12.4	9410_2742	...	CHX 15b	...	...	★
41	W	2	5	15.8	...	T43	Sz 33	...	...	★
42	W	1	4	...n	...	T41	HD 97300	P92	FSC	
43	C	1	5	12.9	...	T45	WX Cha	P92	FSC	
44	C	1	5	...nd	9410_0364	T44	WW Cha	P92	P92,GS92	
45	W	1	3	...n	...	T45a	GK-1	...	GS92	
46	C	1	2	12.2	9410_2682	T46	WY Cha	P92	P92,GS92	
47	New	1	5	13.0	...	...	...	S92	FSC	★
48	New	1	2	13.2	9410_0038	...	...	...	...	
49	New+W	2	20	...	...	...	(see note)	...	FSC	★
50	W	1	1	...	...	T51	Sz 41	P92	FSC	★
51	C	1	2	9.5	9410_0060	T52	LkHα332-21	P92	FSC	★
52	New	2	7	...	...	...	...	...	...	★
53	New	1	3	13.9	...	...	...	...	...	★
54	W	1	12	12.7	...	...	CHX 21a	...	...	★
55	W	2	3	11.5	9410_0062	...	CHX 20E	...	...	★
56	W	1	3	...n	9414_0209	T54	HM Anon	P92	GS92	
57	New	1	19	13.5	...	...	...	...	...	
58	?	3	...	...	...	...	...	...	...	★
59	New	1	11	13.5	...	...	...	...	...	
60	New	2	11	15.6	...	...	...	...	...	★
61	W	1	4	15.6	...	T55	Sz 44	...	...	
62	New	1	2	15.2	...	...	...	...	...	

TABLE 4—*continued*

CHXR	Class	Reliability	Offset "	ESO R	GSC	Cha I No.	Other Name	Near-IR	Far-IR	Notes
63	?	3	...	...	...	...	...	...	...	★
64	U	1	13	...	...	...	NGC 3620	...	FSC	★
65	New	1	10	12.6	9414_0450	...	...	...	...	
66	C	2	12	12.9	9914_0380	T56	HM 32	P92	FSC	★
67	?	3	...	...	...	...	...	...	...	
68	New	2	20	12.2d	...	...	...	...	...	★
69	New	2	...	...	...	...	...	...	...	★
70	New	2	...	...	...	...	...	...	...	★
71	New	1	13	14.6	...	...	...	...	...	★
72	New	2	14	14.2	...	...	...	...	...	★
73	New	1	9	18.2	...	...	...	...	...	
74	New	1	10	16.0	...	...	...	...	...	★
75	W	2	12	13.7	...	T24	UZ Cha	P92	FSC	★
76	New	1	7	16.7	...	...	...	...	...	
77	?	3	...	...	...	...	...	...	...	★
78	New	2	18	...	...	...	...	...	...	★
79	New	1	5	17.2	...	...	...	S92	...	★
80	?	3	...	...	...	...	...	...	...	
81	?	3	...	...	...	...	...	...	...	
82	C	1	5	13.9	9410_0512	T48	WZ Cha	...	...	
83	?	3	...	...	...	...	...	...	...	
84	?	3	...	...	...	...	...	...	...	★
85	W	2	5	15.6	...	T50	Sz 40	...	...	
86	?	3	...	...	...	...	...	...	...	
87	?	3	...	...	...	...	...	...	...	
88	?	3	...	...	...	...	...	...	...	
89	?	3	...	...	...	...	...	...	...	

NOTES.—Star Class: C = Classical T Tauri (EW[Hα] > 10 Å or $I_\alpha \geq 3$; see Table 6); W = Weak T Tauri (EW[Hα] < 10 Å or $I_\alpha \leq 2$; see Table 6); New = probable New weak T Tauri; U = Unrelated to the cloud; ? = Identification very uncertain. Reliability: 1 = certain or very probable stellar identification; 2 = probable stellar identification, but exact counterpart is ambiguous; 3 = identification uncertain or unknown. ESO *R*: R = magnitude from our photographic photometry (Appendix A); n = nebulous on the ESO plate; d = double on the ESO plate and/or reported double by Chen & Graham 1992. Cha I name: T designation from Whittet et al. 1987 with modifications by Schwartz 1992. Infrared identifications: FSC = *IRAS* Faint Source Catalog, v. 2.0; GS92 = Gauvin & Strom 1992 analysis of *IRAS* images; P92 = Prusti et al. 1992 ground-based photometry and *IRAS* analysis; S92 = Schwartz 1992.

from FK89, and the offset between the *ROSAT* and *Einstein* source positions (cols. [10]–[11]); and reference to notes following the tables (col. [12]).

3. STELLAR IDENTIFICATIONS

3.1. *Optical Counterparts*

The search for stellar counterparts of the *ROSAT* sources was conducted using three complementary resources: (1) published compilations of cloud members, including photometric variables, Hα emitters, infrared and *Einstein* X-ray sources (Whittet et al. 1987; S92; GS92); (2) the Guide Star Catalog (GSC) Version 1, listing nearly all stars brighter than ~15th magnitude, constructed at the Space Telescope Science Institute (Lasker et al. 1990); and (3) inspection of digitized *J*-band Schmidt plates from the southern ESO/SERC Sky Survey. Finding charts for each of the 89 sources from these plates are shown in Figure 4 (Plates 21–25). Their digitization procedure and astrometric, and photometric analysis were obtained with the MAMA automatic microdensitometer at the Observatoire de Paris, as described in Appendix A.

The basic criterion for optical identification is that the proposed star falls inside the boresight-corrected *ROSAT* 90% confidence error circle. The finding charts are an essential tool for this, and readers are invited to examine the stellar environment of the X-ray sources from the finding charts. In the majority of cases, a single optical star lies in the error circle. In other cases, multiple identifications are possible, and sometimes no clear stellar candidate is evident. The stellar identification effort is summarized in Table 4. It gives the offset between the *ROSAT* centroid and MAMA star position, when a unique identification is evident (col. [4]); the MAMA *R*-band magnitude (col. [5]); the Guide Star Catalog identification if applicable (col. [6], the first four digits give the GSC region number and the last four digits the star number); the cloud membership number from Whittet et al. (1987) and S92 (col. [7]); the common name of the star (col. [8], usually from GS92); identification with infrared sources (cols. [9]–[10]); and reference to the extensive notes on individual sources (col. [11]). These notes can be found in Appendix B.

We attempt to consolidate the diverse information in Table 4, the finding charts and explanatory notes in Appendix B, into two indicators: stellar "class" (col. [2]) and identification "reliability" (col. [3]). The first indicator divides the proposed counterparts into five classes: "C" for previously known classical T Tauri stars, "W" for previously known weak T Tauri stars, "New" for proposed new T Tauri stars, "U" for objects unrelated to the cloud (e.g., foreground stars or background galaxies), and "?" for sources unclassified for lack of information. The distinction between CTT and WTT is here made solely on the basis of existing Hα line equivalent widths EW(Hα) (>10 Å and <10 Å, respectively) and does not take

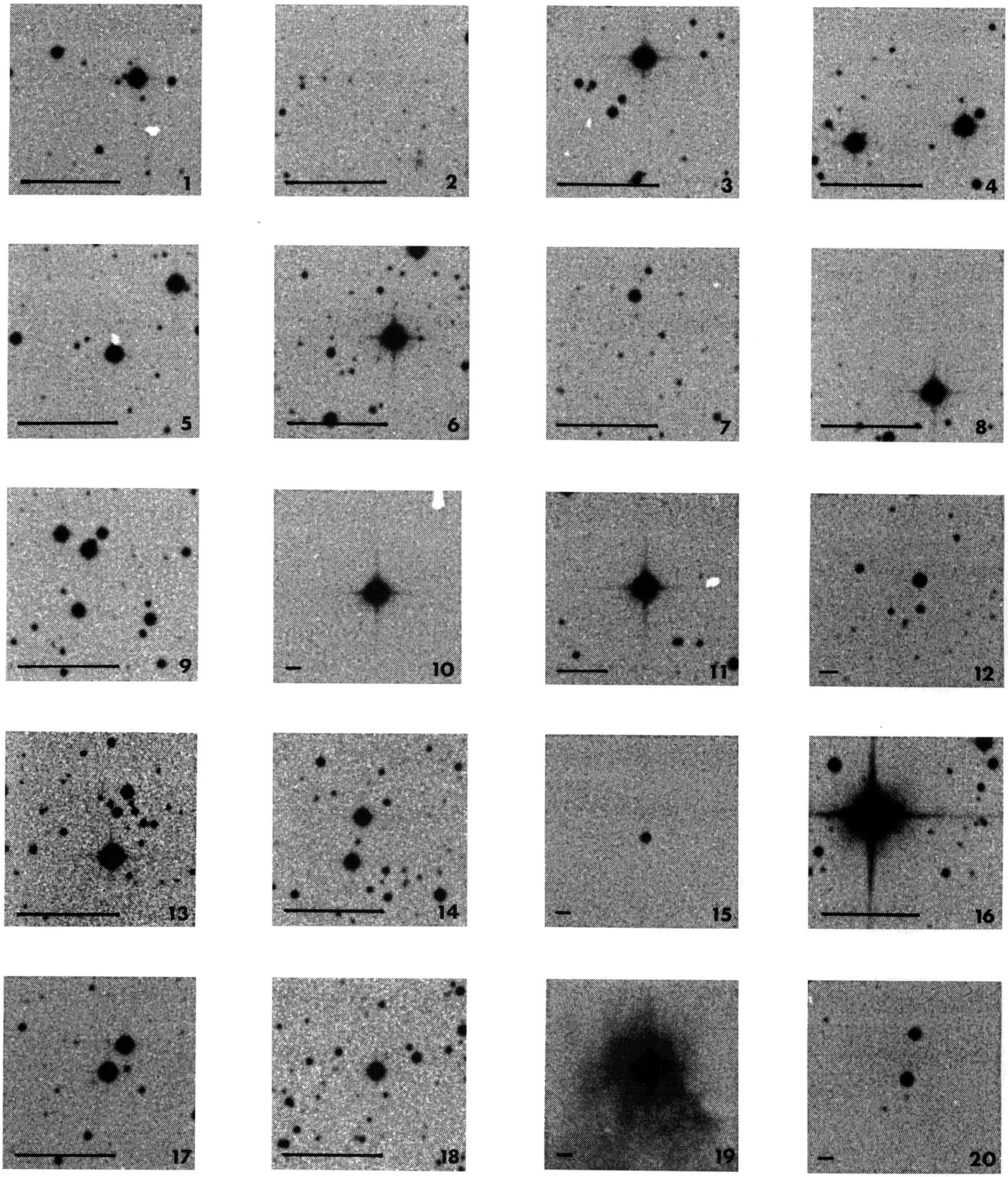

FIG. 4.—Optical finding charts of the 89 *ROSAT* sources in Tables 2 and 3, from the MAMA digitization of the ESO/SERC Sky Survey *J*-band plate (see Appendix A for details). Each chart is 2′ × 2′, with north at the top and east at the left, centered on the boresight-corrected *ROSAT* position. The bar at the lower left indicates the diameter of the *ROSAT* 90% confidence error circle.

PLATE 22

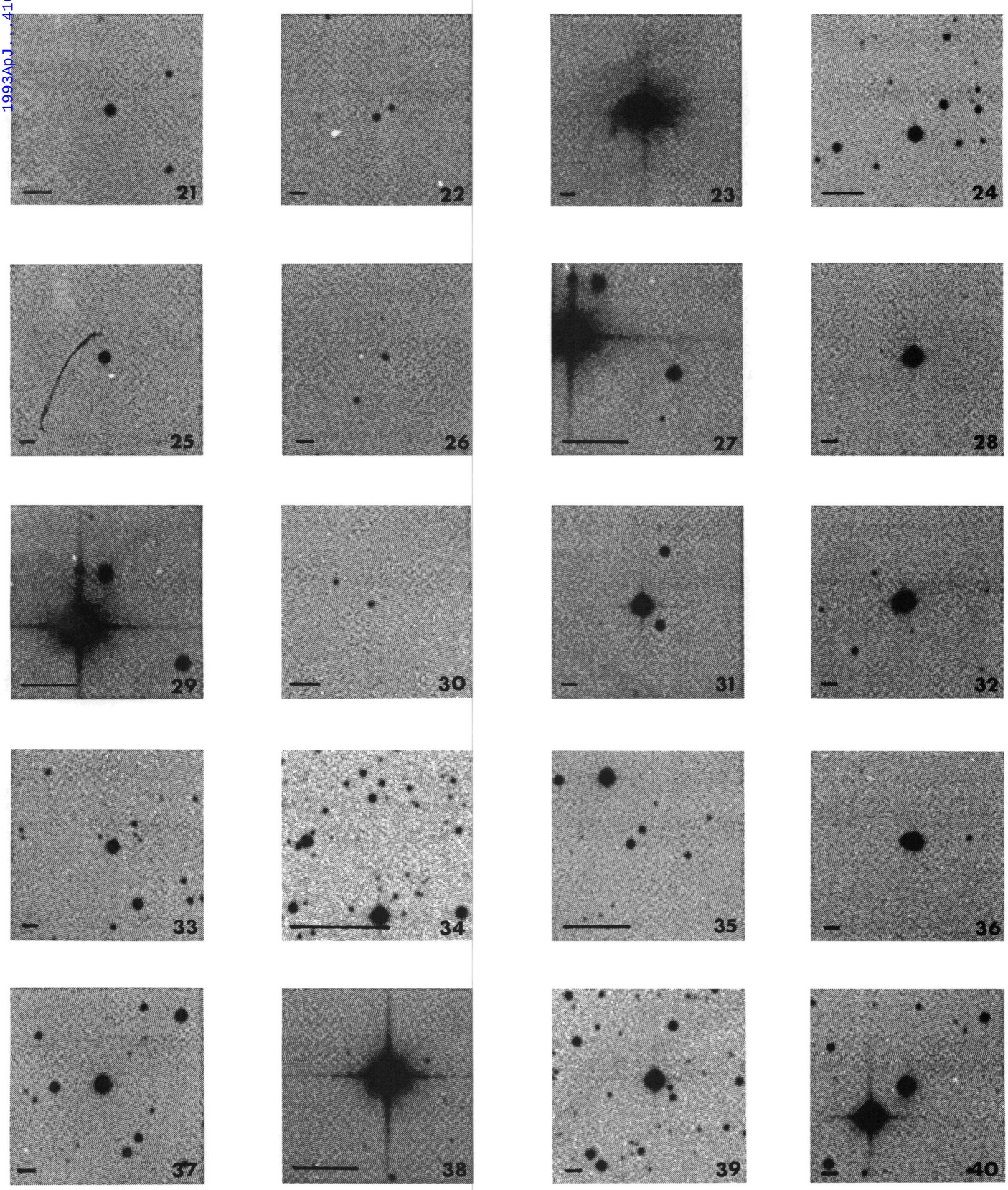

FIG. 4—*continued*

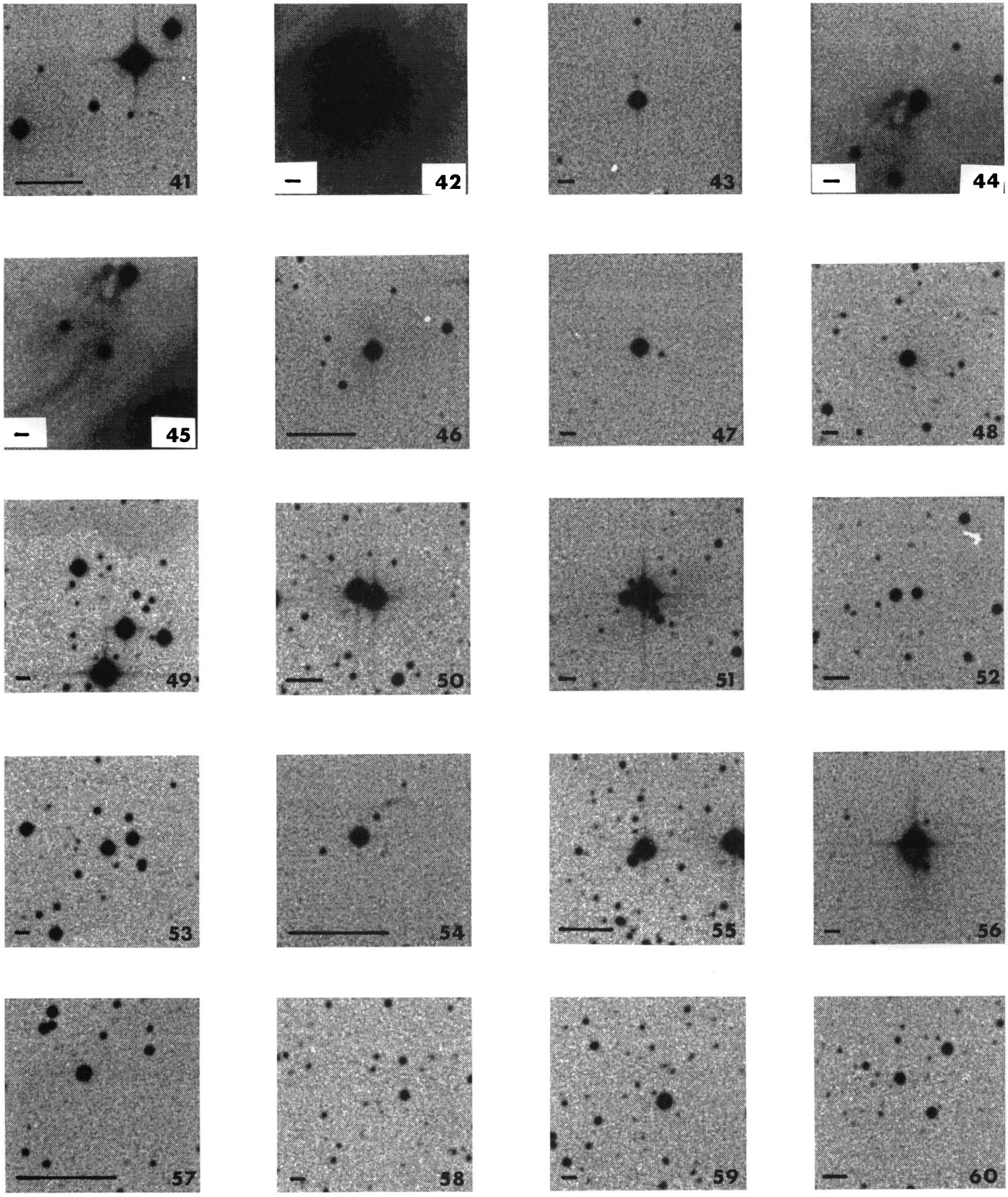

FIG. 4—*continued*

PLATE 24

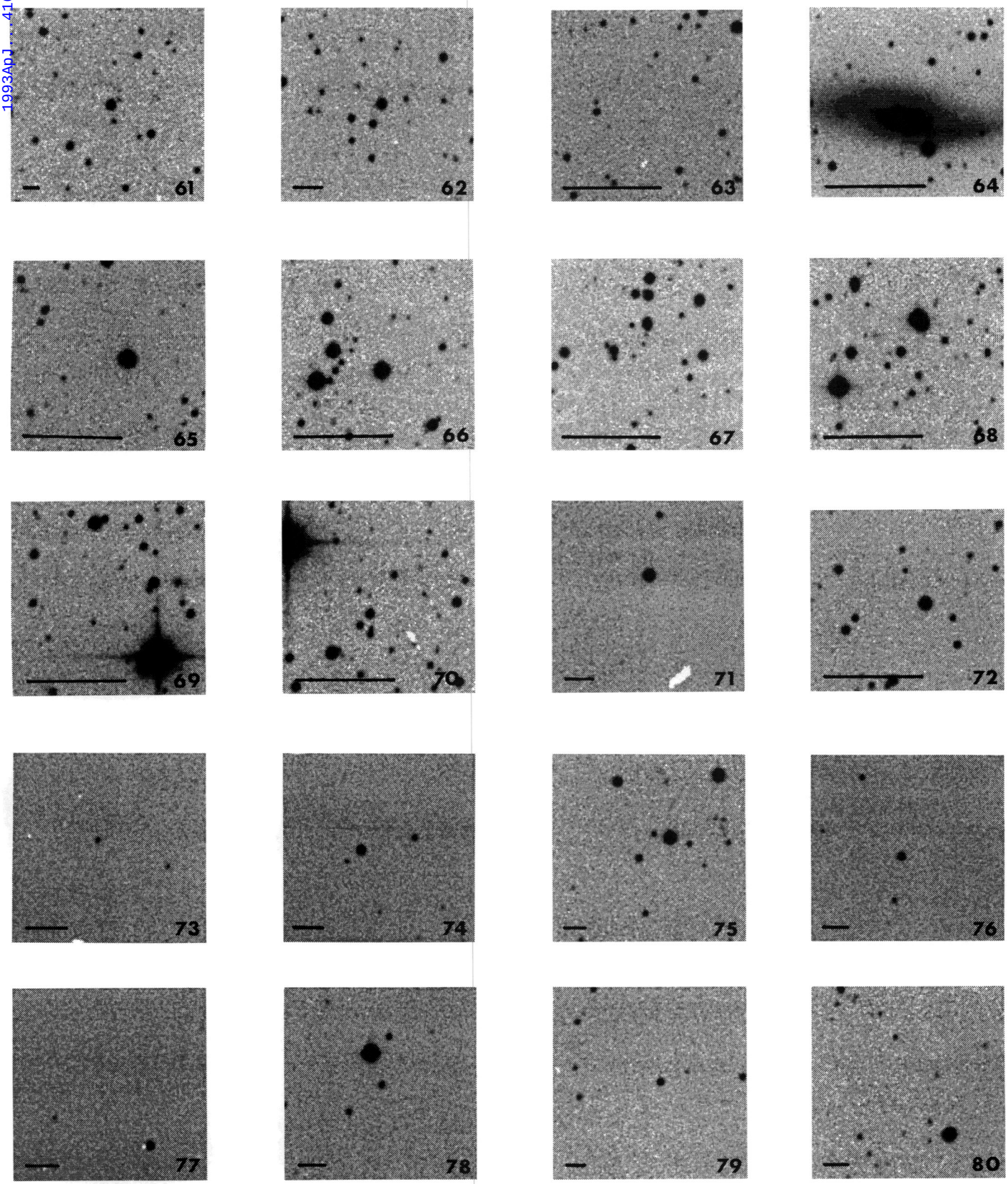

FIG. 4—*continued*

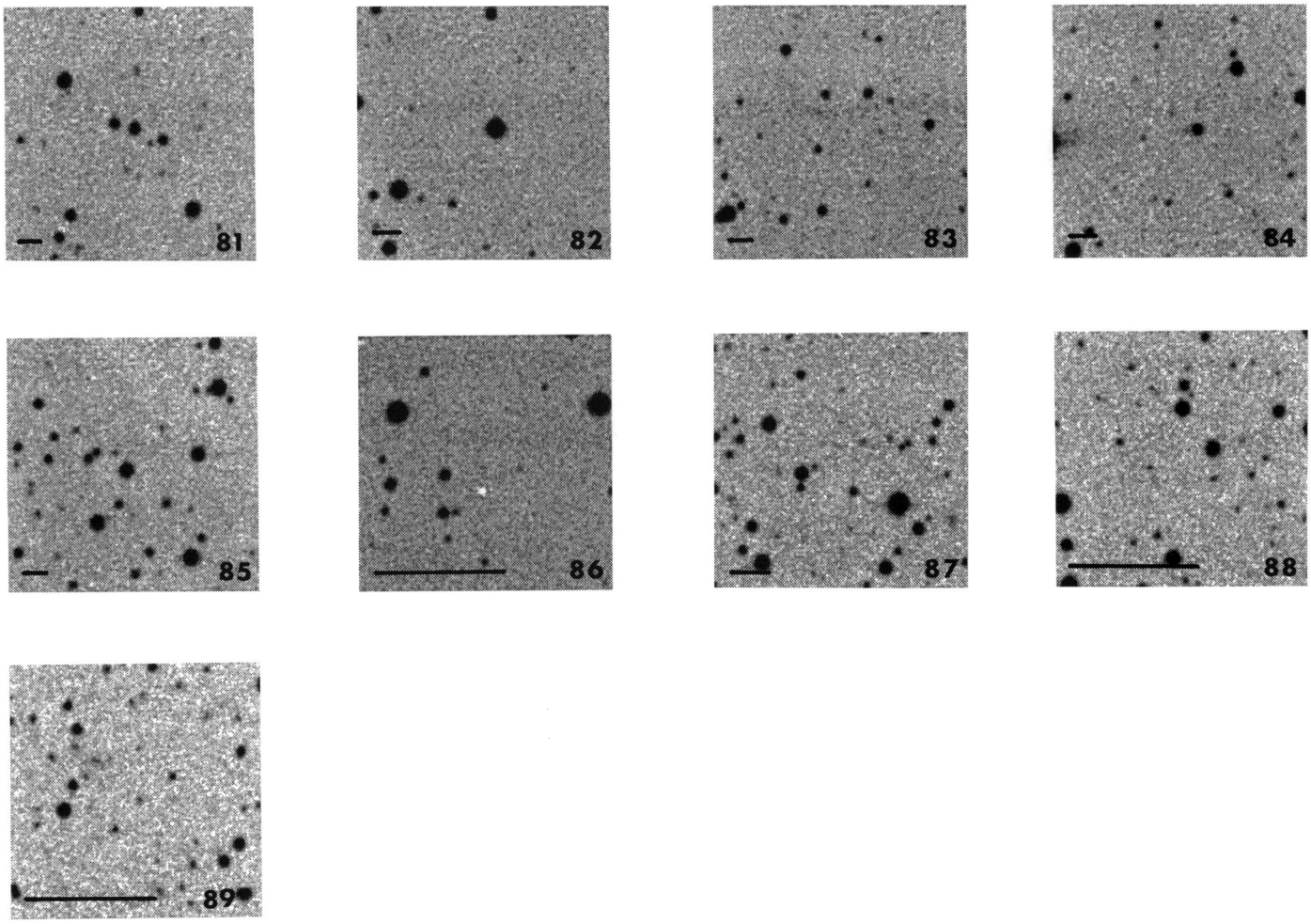

FIG. 4—*continued*

FEIGELSON et al. (see 416, 630)

into account other important properties such as infrared excess or optical/UV veiling. For a number of stars, however, only the Hα intensity classes I_α from Schwartz's (1977) sensitive Hα survey are available; in these cases, WTT stars are defined to have $I_\alpha \leq 2$, and CTT stars to have $I_\alpha \geq 3$. It should be stressed that the Hα line is frequently time variable, so that it is possible that some stars with EW(Hα) ≈ 10 Å may be classified either as CTT or WTT depending on the epoch of observation. Note that, given this definition of CTT and WTT stars, a considerable number of WTT stars are present in Schwartz's (1977) survey and in the photographic variable star study of Hoffmeister (1963).

The second indicator in Table 4 gives our evaluation of the reliability of each X-ray source identification. When a single object falls inside or just adjacent to a small X-ray error circle, we give a high reliability indicator of "1." We also list high reliability when one star is much brighter than others in the error circle. We list reliability indicator "2" when the error circle is large and has more than one plausible stellar identification, when the likely identification is a visual binary unresolved by *ROSAT*, or when the nearest prominent star lies significantly outside the error circle. The low reliability class "3" is assigned to crowded fields where the identification is very uncertain or unknown. The star class and reliability indicators are necessarily preliminary, and will be improved by follow-up observations.

3.2. *Infrared Identifications*

In addition to optical band identifications, infrared counterparts of the X-ray sources are important for two reasons. First, the infrared luminosity of T Tauri stars is often dominated by a dusty circumstellar disk and is thus an indicator of the star formation process and disk evolution. Second, X-ray sources could be identified with stars embedded deeply in the molecular cloud where optical emission is absorbed. Since absorption of soft X-ray emission accompanies optical obscuration, the association of a *ROSAT* source with an embedded star would imply an unusually strong X-ray luminosity.

Ground-based near-infrared observations (≤ 10 μm) give the most reliable identifications since they have positional accuracies of a few arcsec or better. S92 and P92 list near-IR sources discovered in the course of several surveys. Twenty-five coincidences between *ROSAT* and near-infrared sources found to be counterparts to the X-ray sources are indicated in col. (9) of Table 4. All except three (CHXR 35, 47, and 79) are associated with previously identified CTT and WTT stars.

Identifications at far-infrared wavelengths (12–100 μm) are made using *IRAS* observations, although the angular resolution is poor at the longer wavelengths and confusion is possible in crowded regions. S92, GS92, and P92 provide lists of *IRAS* sources associated with the Cha I cloud. We have also cross-correlated X-ray positions with version 2.0 of the *IRAS* Faint Source Catalog (FSC; Moshir et al. 1992). This catalog is a superset of the *IRAS* Point Source Catalog, with a factor of ~2.5 higher sensitivity and typical positional accuracies of 10″ × 2″ (1 σ) at 12 μm. Coincidences were determined by overlapping *ROSAT* and *IRAS* error ellipses and are indicated by "FSC" in column (9) of Table 4. Twenty-four previously known coincidences with optically identified CTT and WTT stars were recovered, and three *IRAS* counterparts of X-ray–selected stars were found: the optically bright WTT stars CHX 18N (CHXR 49), and two "New" stars (CHXR 30, 47). See Appendix B for details. We suspect these last two stars are intrinsically luminous WTT or CTT stars that suffer considerable reddening due to cloud dust along the line of sight.

3.3. *Herbig-Haro-Object Identifications*

Cross-correlation of the 89 X-ray locations with the positions of Herbig-Haro objects 48–51 (Schwartz 1977) and the Infrared Nebula (probably a reflection nebula; Schwartz & Henize 1983) produced no coincidences. There is thus no indication of X-ray emission with $\tilde{L}_X > 6 \times 10^{28}$ ergs s^{-1} from large-scale ejecta of T Tauri stars in the Chamaeleon I cloud.

4. OVERVIEW OF THE X-RAY SOURCE POPULATION

4.1. *Summary of Results*

The analysis of the two *ROSAT* Chamaeleon images reveals 70 X-ray sources detected with confidence (Table 2), having 2 to nearly 500 PSPC counts ks^{-1}, or $\tilde{L}_X \simeq 0.6$ to 140×10^{29} ergs s^{-1}. Nineteen additional sources with low S/N ratios are listed; half of these have no obvious optical counterparts and are probably spurious. The integrated X-ray emission of all the sources probably associated with the cloud (i.e., the 73 C, W, and New stars in Table 4) is 5×10^{31} ergs s^{-1}. Table 5 gives a brief summary of the likely stellar origin of the *ROSAT* sources, based on the "Class" and "Reliability" indicators of Table 4. The summary shows that similar numbers of previously known CTT and WTT stars are detected, about 15 of each type.

A large number of "New" stellar counterparts are also identified: 19 New stars are detected with high reliability, and up to 20 more may be present when low-significance X-ray sources and Reliability 2 identifications are included. Few of the New stars will have CTT properties (the faint highly obscured stars are possible exceptions), since they did not appear in Schwartz's (1977) sensitive and spatially complete Hα survey. Most, we believe, will be new WTT stars (see § 4.2). If we combine the WTT and New proposed identifications, the X-ray–emitting WTT + New population exceeds the X-ray–

TABLE 5

SUMMARY OF PROPOSED X-RAY IDENTIFICATIONS

	CTT Stars Reliability		WTT Stars Reliability		New Stars Reliability			
Sample	1	2	1	2	1	2	Unrelated	Unknown
70 strong *ROSAT* sources	13	4	9	5[a]	19	13[a]	4	4
89 *ROSAT* sources	14	4	9	7[a]	24	15[a]	4	13

[a] The extended source CHXR 49 is counted here as both a WTT and a new identification.

emitting CTT population by a factor of ~ 3 (Table 5; the exact value depends on the source and reliability samples used). This result confirms the conclusions of *Einstein*-era studies (e.g., Walter et al. 1988; FK89; Strom et al. 1990) that weak T Tauri stars numerically dominate classical T Tauri stars during the pre–main-sequence evolutionary phase.

To complement this summary of *detected* stars, it is helpful to consider also the pre–main-sequence stars that are *not detected*. Table 6 reproduces the census of well-characterized optical cloud members compiled by GS92 with a few additions and deletions (see notes to col. [1]). Considering only the detected fractions here (and including low S/N sources and reliability 2 identifications), we find that 34 of 60 (55%) of previously known cloud members are detected. Taken at face value, the fractions of all detected CTT stars (18/30) and WTT stars (16/30) are statistically indistinguishable.

4.2. *Possible Non–Pre–Main-Sequence Contaminants*

While the pre–main-sequence nature of the New stars can not be confirmed until their optical spectra are in hand (such observations are in progress), the fraction which are X-ray–emitting stars unrelated to the cloud can be estimated. Feigelson et al. (1987) discuss the expected rate of coincidence with bright main-sequence (primarily F) stars, RS CVn binaries, dMe flare stars, white dwarfs, and X-ray binaries in an *Einstein Observatory* study of the Taurus-Auriga clouds. A similar analysis of our *ROSAT* fields suggests that few, probably <5, of the New Chamaeleon stars are in these categories. It is possible that two other classes may be present: (1) some of the brighter New stars may be main-sequence B stars; and (2) background active galactic nuclei may be responsible for some *ROSAT* sources with faint ($R \geq 17$) optical counterparts in regions with little obscuration. However, nearly all New stars have $11 < R < 15$ (or, if fainter, are obviously embedded in the cloud), which is expected for pre–main-sequence stars and is largely inconsistent with either B stars or quasars. We thus predict that the great majority of proposed "New" stars are in fact new pre–main-sequence cloud members, with few B, F, dMe, RS CVn-type or extragalactic contaminants.

4.3. *Spatial Distributions of Pre–Main-Sequence Stars*

The spatial distribution of X-ray sources is diagrammed in Figure 5*a*. Figure 5*b* shows the distribution of the previously known optically and infrared-selected pre–main-sequence stars (GS92; S92). Several features can be noted. First, the X-ray–selected stars (Fig. 5*a* minus the "U" and "?" identifications) and optical/IR selected sample (Fig. 5*b*) have very similar total population and spatial distributions. Except for the clusters of infrared sources in the cloud cores from which soft X-ray emission is absorbed, there is no evidence that X-ray selection emphasizes a more dispersed (i.e., older) population than optical selection.

Second, pre–main-sequence stars in the northern portion of the cloud appear as dispersed as those in the southern portion of the cloud, even though the dust distribution in the north is confined to a rather narrow "finger." As the *IRAS* contours in Figure 5 show, this North-South difference is no longer evident if one compares the stellar distributions with the dense cloud cores (solid lines), rather than the less dense outer contours of optical obscuration or far-infrared dust emission (dotted line). Here we see that the young stars are uniformly dispersed within our *ROSAT* fields, that is, distributed $\pm 20'$–$30'$ (1 pc) around cores having radii $\sim 5'$ (0.2 pc). This stellar distribution

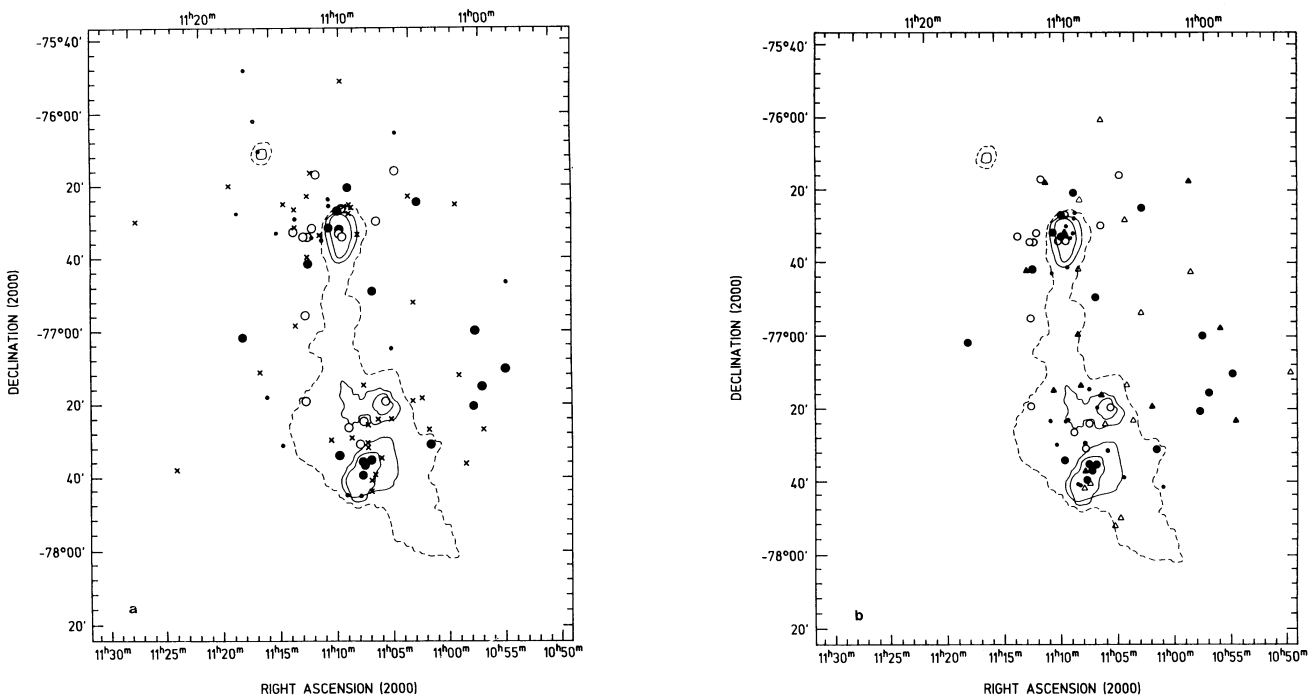

FIG. 5.—(*a*) Diagram of spatial distributions of the 89 X-ray sources. The symbols are from the classifications in Table 4: CTT (*filled circle*), WTT (*open circle*), New (*cross*), and unrelated to the cloud (*dot*). Contours from the *IRAS* 100 μm map show the outer boundary of the cloud (*dashed line*) and the cloud cores (*solid lines*). (*b*) Similar diagram for optical and infrared selected CTT and WTT stars: the same X-ray–detected CTTS (*filled circle*), and WTTS (*open circle*) as in panel (*a*) plus CTT/WTT stars that are undetected in X-rays (*filled/open triangles*) and embedded infrared sources (*dot*).

TABLE 6

PROPERTIES OF CONFIRMED CHAMAELEON I CLOUD MEMBERS

Name	X-ray		A_V	Bulk Star						Circumstellar Material			
	log L_x (erg/s)	log L_x (erg/s)		log T_{eff} (°K)	L_* ($L_\odot$)	R_* ($R_\odot$)	M_* ($M_\odot$)	t_* (Myr)	EW(Hα) (Å)	I_α	Star Class	log $F_{H\alpha}$ ($ergs^{-1}cm^{-2}$)	L_{disk} ($L_\odot$)
Sz 1	<29.5	...	...	...	...	...	...	...	...	1	W	...	...
SX Cha	<29.5	<29.5	1.12	3.580	0.3	1.2	0.8	8	26.7	2	C	7.71	0.4
SY Cha	29.4	29.2	0.21	3.593	0.3	1.2	0.8	15	63.6	2	C	8.15	0.5
Sz 4	<29.5	...	...	...	...	...	...	...	...	3	C	...	...
SZ Cha	29.6	29.7	1.88	3.719	1.7	1.6	1.3	10:	12.0	...	C	8.14	0.7
TW Cha	29.6	30.0	2.99	3.719	0.9	1.1	1.0	20:	26.1	4	C	8.68	0.3
Lk 332-20	30.1	30.2	1.37	3.695	2.4	2.1	1.3	5:	43.6	3	C	8.51	0.7
HM 5	<29.5	...	...	...	...	...	...	...	...	0	W	...	...
HM 6	<29.5	...	...	...	...	...	...	...	...	4	C	...	...
CS Cha	30.1	30.0	0.85	3.661	1.1	1.7	1.2	5:	13.3	...	C	7.84	0.3
HM 8	<28.8	<28.8	1.00	3.580	0.1	0.7	0.7	30:	102.8	3	C	7.95	0.1
TZ Cha	<29.5	...	...	...	...	...	...	...	...	...	W	...	...
CT Cha	29.5	29.3	0.41	3.602	0.6	1.6	0.9	3	49.2	3	C	8.12	0.6
HM 10	<28.8	...	...	...	...	...	...	...	...	0	W	...	...
Sz 13	<28.8	...	...	...	...	...	...	...	...	2	W	...	...
UU Cha	<28.8	...	...	...	...	...	...	...	...	...	W	...	...
Sz 14	<29.5	...	...	...	...	...	...	...	...	1	W	...	...
Sz 15	<29.5	...	...	...	...	...	...	...	...	1	W	...	...
UV Cha	29.9	...	...	...	...	...	...	...	...	...	W	...	...
Ced 110	30.2	30.7	3.39	3.761	11.2	3.3	2.0	1:	<1.2	...	W	7.27	2.8:
UX Cha	<28.8	...	...	...	...	...	...	...	...	...	W	...	...
UY Cha	<28.8	<29.1	2.78	3.555	0.3	1.3	0.6	4	56.3	1	C	7.84	0.3
UZ Cha	28.8	...	...	...	...	...	...	...	...	...	W	...	...
HM 12	<29.5	<29.5	1.20	3.544	0.2	1.1	0.6	6	3.2	2	W	6.52	0.4
Lk 332-17	29.7	29.9	2.35	3.761	7.8	2.8	1.8	3	17.2	1	C	8.37	2.2
VV Cha	29.3	29.3	1.01	3.566	0.3	1.2	0.7	6	74.9	5	C	7.91	0.2
HM 15	29.0	29.2	2.02	3.580	0.3	1.2	0.8	8	47.9	4	C	7.88	1.6
CHX 10a	30.0	30.6	3.72	3.643	4.2	3.5	1.5	0.5:	0.2	...	W	...	...
HM 16	<28.9	...	...	...	...	...	...	...	...	4	C	...	...
Sz 23	<28.8	...	...	...	...	...	...	...	...	1	W	...	...
VW Cha	30.0	30.3	2.39	3.643	1.8	2.3	1.3	1:	146.9	4	C	8.80	1.4
HD 97048	28.9	29.0	1.30	4.009	18.6	1.4	...	...	30.0	1	C	9.48	8.6
Glass Ia	29.9	30.1	1.92	3.661	1.1	1.7	1.2	10:	4.0	...	W	...	2.9:
HM 19	<28.8	<28.9	1.70	3.518	0.2	1.4	0.3:	2:	5.0	0	W	6.40	0.0
HM 20	<28.8	<29.1	2.70	3.593	0.2	0.9	0.8	20:	81.8	4	C	8.23	0.2
VX Cha	<28.8	...	...	...	...	...	...	...	...	...	W	...	...
Sz 28	<28.8	...	...	...	...	...	...	...	...	2	W	...	...
VY Cha	<29.5	<30.2	5.00	3.580	0.2:	1.1	0.7	20:	55.1	4	C	8.37	0.4:
Sz 30	30.1	30.1	1.18	3.593	0.7	1.8	0.8	2	5.2	1	W	...	...
VZ Cha	29.6	29.5	0.47	3.623	0.3	1.0	0.9	30:	71.4	4	C	8.44	1.0
HD 97300	29.0	29.2	1.80	4.025	14.6	1.1	...	...	0.0	...	W	...	15.7:
HM 23	<28.8	...	...	...	...	...	...	...	...	4	C	...	...
Sz 33	28.8	28.9	1.45	3.593	0.4	1.3	0.9	8	9.5	1	W	...	0.9
WW Cha	29.4	29.8	3.20	3.643	1.9	2.4	1.2	3:	67.4	3	C	8.48	16.7:
WX Cha	29.5	29.7	2.14	3.598	0.3	1.2	0.9	10:	65.5	3	C	8.23	0.6
GK-1	29.6	29.8	1.95	3.593	0.2	1.1	0.8	30:	0.0	...	W	7.13	6.8:
WY Cha	29.7	29.9	1.79	3.602	0.5	1.4	0.9	6	56.3	4	C	8.19	0.7
HM 27	<28.8	<29.3	3.40	3.602	0.1:	0.8	0.7	30:	200.9	3	C	9.25	0.4:
WZ Cha	28.6	28.6	1.47	3.566	0.1	0.9	0.7	20:	388.2	5	C	8.70	0.2
XX Cha	<28.8	<28.6	0.61	3.566	0.1	0.8	0.7	30:	133.5	5	C	8.27	0.5
CHX 18N	<30.6	<30.8	2.17	3.709	...	...	...	...	7.6	...	W	...	...
Sz 40	28.6	...	...	...	...	...	...	...	...	2	W	...	...
Sz 41	30.2	30.2	1.17	3.714	1.2	1.3	1.1	10:	2.7	1	W	7.44	0.3
Lk 332-21	30.0	30.1	1.67	3.736	3.4	2.0	1.5	10:	60.5	3	C	8.85	0.9
CW Cha	<28.8	<28.9	1.36	3.580	0.2	1.1	0.7	20:	33.3	4	C	7.74	0.1
CHX 21a	29.7	29.8	1.24	3.643	0.5	1.1	1.0	20:	1.0	...	W	...	...
HM Anon	30.5	30.5	1.21	3.736	1.9	1.5	1.3	20:	1.5	...	W	7.27	2.0:
CHX 20E	29.6	29.4	0.31	3.643	...	...	...	...	0.0	...	W	...	...
Sz 44	29.3	...	...	...	...	...	...	...	...	1	W	...	...
HM 32	30.0	29.8	0.23	3.580	0.3	1.2	0.8	10:	31.9	3	C	7.72	0.1

Col. (1): Sample from Table 1A of GS92, with three deletions (SW Cha and T Cha lie outside the *ROSAT* fields, and the exciting star of the Infrared Nebula is not optically visible) and four additions from the *Einstein* CHX sources with confirmed cloud membership (W92).

Col. (2): Approximate log X-ray luminosity in the *ROSAT* 0.4–2.5 keV band, based on the count rate conversions given in § 2. Upper limits for the nondetections are assigned as described in § 2, except for HM 16 and CHX 18N. Here, due to uncertain stellar identifications of the X-ray source (see Table 4, notes to sources 29 and 49), the upper limits are set equal to the detected X-ray level.

Col. (3): More accurate log X-ray luminosity, based on a fit of the observed PSPC pulse height photon distribution with an assumed 1 keV thermal plasma subject to absorption scaled to A_V in col. (4). See § 2.3 for details.

Col. (4): Visual absorption, calculated by GS92 from optical and infrared photometry.

Col. (5): Log effective temperature, obtained from the spectral type following GS92 and Strom et al. (1989).

Col. (6): Bolometric luminosity of the star from GS92 Table 2 (corrected to $d = 140$ pc) where available. For CHX stars, luminosities are calculated from the spectral types and color excesses of W92 (where available) or FK89 and the photometry of FK89, assuming no disk contribution at V or R bands. Giant star bolometric corrections are adopted from Allen (1973).

Col. (7): Radius of the star assuming a blackbody, calculated from cols. (5) and (6).

Cols. (8) and (9): Mass and age of the star, based on cols. (5) and (6), estimated from the theoretical pre–main-sequence Hertzsprung-Russell diagram isochrones plotted in Strom et al. (1989). Values estimated by visual interpolation; extrapolated values are indicated by a colon.

Col. (10): Equivalent width of Hα from GS92 and (for CHX stars) from FK89 and W92. Note that Hα can be highly variable in many of these stars.

Col. (11): Indicator of Hα strength from Schwartz 1977, derived from objective prism plates. The 0–5 scale increases with Hα brightness.

Col. (12): Classification derived from cols. (10) and (11). In most cases, C (classical T Tauri) indicates EW(Hα) > 10 Å and Schwartz indicator 3–5, and W (weak T Tauri) indicates EW(Hα) < 10 Å and Schwartz indicator 0–2. The EW(Hα) criterion is chosen in case of classification conflict with I_α. The CHX stars, which have EW(Hα) < 10 Å but no Schwartz indicator, are assigned W.

Col. (13): Bolometric luminosity of the infrared excess, attributed to the circumstellar disk, from GS92.

is similar to that found around dense cores within giant molecular clouds (Lada 1992; see § 8 below).

Third, and perhaps most important, the spatial distributions of CTT, WTT, and proposed New stars do not clearly differ in any respect. There is no indication that CTT stars lie closer to the dense cores than WTT or New stars, as might be expected if they formed more recently. This null result is confirmed by a simple quantitative analysis. Choosing a circle 8′ in radius centered on the cloud cores shown in Figures 5 to discriminate between the "inner" and "outer" regions, we find 7:11 (X-ray CTT stars), 6:10 (X-ray WTT stars), 15:24 (X-ray New stars), 10:20 (previously known CTT stars), and 9:21 (previously known WTT stars) in the inner:outer regions.

The similar spatial distributions of CTT and WTT stars cannot be due to spatially distributed star formation, because a spatial segregation is clearly seen when stellar age, rather than CTT-WTT classification, is examined. Using stellar ages estimated from Hertzsprung-Russell diagram isochrones (see § 6 and Table 6 below), we find that stars within the *IRAS* cores have a mean age $\langle t_* \rangle = 7 \pm 2 \times 10^6$ yr, while stars outside of these cores have $\langle t_* \rangle = 15 \pm 2 \times 10^6$ yr. A few older stars also lie on the dense cores, but these may lie far from the cores along the line of sight. A similar age segregation of T Tauri stars was found by Walter et al. (1988) in the Taurus-Auriga complex.

These results confirm the mixing in age between CTT and WTT stars which was already apparent from their positions on the Hertzsprung-Russell diagram (see Fig. 2 in GS92). It suggests that some stars are "born" as WTT stars, and/or that the lifetime of CTT star-disk interactions can be as short as $< 1 \times 10^6$ yr or as long as several $\times 10^7$ yr. This issue is discussed in more detail by Skrutskie et al. (1990) and Montmerle & André (1989) and in § 8 below.

4.4. *Comparison with Einstein Observatory Results*

All of the 22 *Einstein* IPC X-ray sources reported by FK89 (except for the weak source CHX 5 which FK89 correctly believed was spurious) are recovered in the deeper *ROSAT* images. The majority of the sources show fluxes quite similar to each other in the two instruments, within 50%. However, a few are factor >2 higher in the *Einstein* (CHXR 1 = CHX 1, CHXR 19 = CHX 7, CHXR 36 = CHX 14) or *ROSAT* (CHXR 6 = CHX 3, CHXR 28 = CHX 10, CHXR 56 = CHX 22) exposures, respectively, suggesting flare activity.

Perhaps the most dramatic difference between the two satellite instruments is the effect of the improved angular resolution of the *ROSAT* telescope. The various remarks in the notes to Table 2 in FK89, hinting at extent or multiple structure in several *Einstein* IPC sources, are now understood from the *ROSAT* images. The "elongated" source CHX 15 is now seen to consist of the string of *ROSAT* sources CHXR 35, 37, 40, 41, and 46. Similarly, CHX 9 may include CHXR 23, 27, and 29; CHX 16 convolves CHXR 42, 44, and 45; CHX 19 includes CHXR 51 and 52; and CHX 20 probably includes CHXR 50 and 55. The modest angular resolution of the *Einstein* IPC thus significantly underestimated the total number of X-ray–emitting young stars, and, by combining several faint sources into one luminous one, overestimated the upper end of the X-ray luminosity function. *ROSAT* alleviates these two problems, as well as resolving most of the ambiguities in *Einstein* proposed optical identifications.

Another difference lies in the higher sensitivity of *ROSAT*. The faintest S/N > 3.5 *ROSAT* sources have luminosity around 6×10^{28} ergs s^{-1} (0.4–2.5 keV band), more than 10 times more sensitive (when the different bandwidths are considered) than the 5×10^{29} ergs s^{-1} (0.2–4 keV band) limit of the IPC fields. Luminosity functions are therefore extended to the lower end by an order of magnitude. An important consequence of the corrected estimation of the upper end, and of the extension of the lower end, of the luminosity function, is that the mean luminosity of the corresponding sample of sources is automatically reduced in a significant manner with respect to values found with *Einstein*. This point must be taken into account when comparing global *Einstein* and *ROSAT* results, as emphasized in the following sections.

5. X-RAY LUMINOSITY FUNCTIONS OF T TAURI STARS

The distribution of X-ray luminosities of pre–main-sequence stars can be an important statistical tool for quantifying the stellar population and for comparing subpopulations. For the *ROSAT* detected stars, the luminosity function can be represented by a simple plot of the number fainter than a given luminosity. Figure 6*a* shows the integrated distributions of the log of the approximate luminosity $\tilde{L}_X$ for the 72 *ROSAT* sources (89 in Tables 2 and 3, minutes 17 with "U" or "?" classification in Table 4), with the CTT, WTT, and New subsamples plotted separately. The mean log luminosities are $\langle \log \tilde{L}_X(\text{ergs s}^{-1}) \rangle = 29.4$, 29.6, 29.6, and 29.3 (all ± 0.1) for the total, CTT, WTT, and New samples, respectively.[6] The distributions are quite narrow: half of all sources lie within a factor of ± 2 of these mean values.

Wilcoxon and logrank nonparametric two-sample tests (e.g., Daniel 1989; Koch, Sen, & Amara 1982) applied after normalizing the luminosity functions, indicate that there is no statistically significant difference between CTT and WTT stars. The New sources, however, have significantly lower X-ray luminosities than the WTT subsample by a factor of 2–4 (>99% confidence level). This difference is even more evident (factor of 4, >99.9% confidence level) when only Reliability Class 1 identifications are considered. We suggest that the lower X-ray luminosities of New stars is not intrinsic, but is due to a selection effect. Many of the New stars are optically fainter than the well-studied WTT and CTT stars, and are fainter in X-rays due to a strong correlation between X-ray and optical flux (Fig. 8*a* below).

While these mean log luminosities are useful for the comparison of subsamples within our study, we caution against their use as absolute measures of the X-ray population or comparison with other studies. As mentioned above, the survey sensitivity increases from *Einstein* to *ROSAT* levels, and the calculated mean luminosity is likely to decrease as more fainter sources are discovered. Furthermore, we have no knowledge of the distribution below about $\langle \log \tilde{L}_X \rangle = 28.5$, and there is no reason to believe that the actual luminosity function stops at this instrumental sensitivity limit. More precisely, the sample of X-ray–detected stars shown in Figure 6*a* might be biased toward high-L_X compared to the general population of Chamaeleon I T Tauri stars, because undetected low X-ray luminosity stars are omitted. We can investigate this potential bias by calculating the Kaplan-Meier estimator of the luminosity function for samples of pre–main-sequence stars selected independent of their X-ray emission. We draw our sample of X-ray unbiased T Tauri stars from the compilation of 40 optically

[6] We follow most previous stellar X-ray studies in comparing mean log luminosities ($\langle \log \tilde{L}_X \rangle$) rather than mean luminosities ($\langle \tilde{L}_X \rangle$).

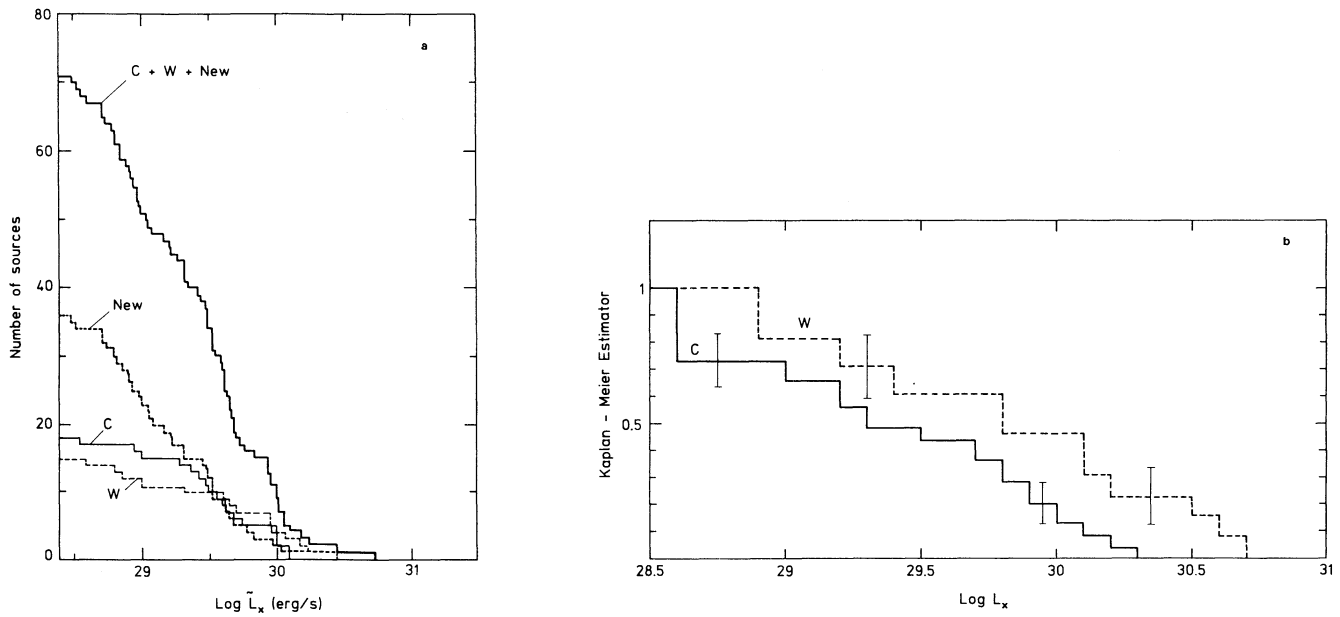

FIG. 6.—(*a*) Integral X-ray luminosity function of the *ROSAT* sources associated with known or proposed T Tauri (*solid heavy line*), and for three subsamples: CTT stars (*light solid line*), WTT stars (*long-dash line*), and proposed "New" T Tauri stars (*short-dash line*). $\tilde{L}_X$ (in ergs s^{-1}) is an approximate X-ray luminosity based on the PSPC count rate. (*b*) Kaplan-Meier maximum-likelihood X-ray luminosity functions of well-characterized CTT and WTT stars. L_X (in ergs s^{-1}) is based on spectral fits corrected for foreground absorption.

selected cloud members in Table 6, and use the absorption-corrected X-ray luminosities described in § 2.3.

Figure 6*b* shows the resulting maximum-likelihood–estimated X-ray luminosity functions. The mean luminosities are $\langle \log L_X \rangle = 29.8 \pm 0.2$ for the WTT stars and 29.4 ± 0.1 for the CTT stars. Nonparametric two-sample tests implemented in ASURV (the Gehan, logrank, Peto-Peto and Peto-Prentice tests) indicate the difference is only marginally significant at a $P = 9\%$–13% confidence level. We note that Damiani, Micela, & Vaiana (1991) found that a sample of 31 WTT stars are stronger than a sample of 22 CTT stars in the Taurus-Auriga clouds at a much higher confidence level of $P = 0.2\%$, based on *Einstein* data. But we caution that the slightly higher mean X-ray levels of WTT stars is likely to disappear when the large number of suggested New identifications, which generally have lower L_X (Fig. 6*a*) and are probably frequently WTT stars (§ 4), are optically characterized and added to the sample. We conclude that there is little evidence that Chamaeleon WTT and CTT stars have systematically different X-ray luminosity distributions.

6. STELLAR X-RAY EMISSION MECHANISM

6.1. *Dynamo Effect and Choice of the X-Ray Variable*

Having identified most of the *ROSAT* sources with young, low-mass stars of the T Tauri family, we can investigate the cause of their high levels of X-ray emission. Based on *Einstein Observatory* results, the most frequently advocated mechanism for this emission is based on the analogy with solar X-ray emission: thermal bremsstrahlung from an optically thin plasma at $T \sim 10^7$ K trapped in magnetic loops. The magnetic field is itself thought to be produced by the dynamo mechanism within the stellar interior, generated by a combination of convection and rotation known as the "$\alpha\omega$" mechanism. Discussions of the evolution of stellar magnetic field, and the likelihood that the dynamo mechanism is present in pre–main-sequence stars, can be found in Levy, Ruzmaikin, & Ruzmaikina (1991) and Montmerle et al. (1993). Solar-type activity is considered the source of activity-age-rotation relations well-established in late-type stars. Here we seek empirical evidence for the dynamo mechanism among our *ROSAT* data of Chamaeleon I T Tauri stars, by considering X-ray emission as the magnetic activity indicator and comparing it to other stellar properties.

The spectral and temporal properties of the X-ray emission of our sample of sources requires a detailed analysis, which will be presented in Paper II. But the preliminary spectral study of the strongest sources do support a thermal origin for the X-rays, and the temporal analysis of data spread over several *ROSAT* orbits also establishes the existence of variability, sometimes at high levels. For instance, Table 2 indicates that CHXR 6 is detected at 42 counts ks^{-1} in field 1, but later at 466 counts ks^{-1} in field 2, indicating a very strong flare event.

The primary quantity measured for a given source from *ROSAT* data, once absorption effects and distance are taken into account, is the X-ray luminosity. Another useful quantity is the X-ray *surface flux* $F_X = L_X/(4\pi R_*^2)$. The choice of L_X or F_X as the X-ray variable is particularly important because the surface area decreases by a factor of $\gtrsim 6$ between age $\simeq 1 \times 10^6$ yr and the main sequence (see Fig. 2 of Feigelson et al. 1991). We believe both variables are useful, but for different purposes. L_X should be used when global properties of the star, and its *effects* on its environment, are sought. These include comparison with total luminosity at other bands, wind emission or kinetic power, disk luminosity, integrated emission of a star-forming region, effects of X-rays on the ionization (Silk & Norman 1983) or chemistry (Krolik & Kallman 1983) of the interstellar cloud, effects of the youthful Sun on primeval planetary atmospheres (e.g., Pepin 1989) and meteorites (Hohenberg et al. 1990), and so forth. On the other hand, F_X is

useful for studies of the astrophysical *causes* of X-ray emission, such as the relations between X-ray production and stellar rotation (Bouvier 1990) or Rossby number (Stepień 1988), in the framework of the dynamo mechanism. In the following sections we choose the X-ray variable according to the question under study.

6.2. *Secular Evolution of the X-Ray Emission*

There is long-standing evidence that the strength of various indicators of magnetic activity in late-type stars decrease with stellar age (Skumanich 1972; but see Simon 1992 for a contrary view). The precise nature of the decay of the X-ray emission of young stars has, however, been subject to debate. From *Einstein Observatory* images, Micela and colleagues (Micela et al. 1988, 1990 and Schmitt et al. 1990) have computed maximum-likelihood X-ray luminosity functions of main-sequence stars of various ages, demonstrating a (somewhat noisy) trend of decreasing X-ray luminosity from young clusters on the main sequence to old disk stars. For solar mass G stars, they find mean X-ray luminosities (in ergs s^{-1}) given by $\langle \log L_X \rangle =$ 29.43 for Pleiads, 29.16 for Hyads, 28.41 for Ursa Major stars, and 27.71 for field disk stars (uncertainties range from ± 0.06 to ± 0.17). FK89 reported, also from *Einstein* data, that Chamaeleon I stars extended this trend back into the pre–main-sequence phase, with $\langle \log L_X \rangle = 30.0$, and interpreted this as a power-law relation $L_X \sim t_*^{-0.6}$ analogous to Skumanich's (1972) relation for optical activity tracers on the main sequence. Damiani et al. (1991) arrive at comparable results using similar methods for Taurus-Auriga cloud members.

On the other hand, Walter et al. (1988) and Walter & Barry (1991) consider the dependence of the X-ray fluxes F_X with stellar age for selected stars (without computing maximum-likelihood luminosity functions). They deduce that X-ray emission is high but relatively constant during the pre–main-sequence and early main sequence, and then declines following the exponential relation $F_X \sim \exp(t_*/4 \times 10^8 \text{ yr})$ or $F_X \sim \exp[-2.2(t_*/1 \times 10^9 \text{ yr})^{1/2}]$. Walter & Barry discuss in detail the evidence for exponential decay laws in chromospheric tracers, transition region tracers, and lithium abundance, as well as X-ray flux. The differing conclusions between the two approaches can be partly attributed to the use of different variables and large scatter of the data points; however, maximum-likelihood analyses of well-defined samples are probably more reliable. We can now address the same question with our superior *ROSAT* Chamaeleon I data, using the values of ages t_* and masses M_* estimated from theoretical isochrones in the Hertzsprung-Russell diagram and listed in Table 6.

First we construct a luminosity function from 18 stars with $0.8 \leq M_*/M_\odot \leq 1.2$ (16 detections, two upper limits), limiting the mass to a narrow range to avoid the trend of $\log L_X$ steeply increasing with mass (see § 7). We artificially increase the *ROSAT* $\log L_X$ values by 0.1 to account for the different bandwidths assumed for the *Einstein* (0.2–4 keV) and *ROSAT* (0.5–2.4 keV) luminosities. The result is $\langle \log L_X(\text{ergs s}^{-1}; 0.2\text{–}4 \text{ keV}) \rangle = 29.63 \pm 0.10$ for Chamaeleon I solar-mass stars (having a mean age $\langle t_* \rangle \sim 1 \times 10^7$ yr), 0.37 below that found in the *Einstein* data (FK89). These *ROSAT* findings are therefore consistent with the *Einstein* result that the X-ray emission decreases monotonically toward the main sequence. The combined angular resolution and sensitivity effects mentioned above (§ 4.4) result here in a factor of 2.3 reduction in mean luminosity of *ROSAT* compared to the *Einstein* Chamaeleon analysis. However, until *ROSAT* data of other young clusters (in particular, the Pleaides, $\langle t_* \rangle \simeq 7 \times 10^7$ yr) are completed, an accurate X-ray decay law, either for L_X or F_X, cannot be established.

TABLE 7

CORRELATIONS BETWEEN X-RAY AND OTHER PROPERTIES

Variables	Number of Stars: Detected	Number of Stars: Undetected	Probability[a] of No Correlation
$\log L_X$ vs. $\log v \sin i$	16	0	23%–50%
$\log L_X$ vs. $\log L_*$	26	10	<0.01
$\log L_X$ vs. $\log T_{\rm eff}$	27	11	<0.01
$\log L_X$ vs. $\log R_*$	26	10	<0.01
$\log L_X$ vs. $\log M_*$	26	10	<0.01
$\log L_X$ vs. $\log t_*$	26	10	0.6–2
$\log L_X$ vs. $\log L_{\rm disk}$	23	10	3
$\log F_X$ vs. $\log P_{\rm rot}/\sin i$	15	0	88%–99%
$\log F_X$ vs. $\log F_*$	26	10	0.01–0.03
$\log F_X$ vs. $\log T_{\rm eff}$	26	10	0.02
$\log F_X$ vs. $\log R_*$	26	10	4–9
$\log F_X$ vs. $\log M_*$	26	10	≤0.1
$\log F_X$ vs. $\log t_*$	26	10	61–96
$\log F_X$ vs. $\log F_{H\alpha}$	21	10	52–76

[a] Without the B9 stars HD 97048 and HD 97300.

Second, given the relatively large spread in ages of the Chamaeleon I T Tauri sample ($t_* \lesssim 1 \times 10^6$ yr to several times 10^7 yr; Table 6), we can consider the secular variation of X-ray emission within the whole pre–main-sequence phase, removing the preceding restriction on the stellar masses. Table 7 and Figure 7 show a significant anticorrelation between $\log L_X$ and $\log t_*$ ($P = 0.5\%$–2% confidence level), and no correlation between $\log F_X$ and $\log t_*$ ($P \geq 61\%$ confidence level). We note, however, that most of the ($\log L_X$, $\log t_*$) correlation arises from the three stars with $t_* \lesssim 1 \times 10^6$ yr, which are among the most luminous and massive stars in the sample. The apparent decrease of X-ray luminosity with stellar age thus may be a by-product of a separate relationship between X-ray emission and mass or radius (§ 7.2).

We conclude that, while photometric and spectroscopic data for more Chamaeleon I cloud members are certainly needed, the existing data support *Einstein* findings (FK89; Damiani et al. 1991) of a decay of L_X as t_* increases from the pre–main-sequence into the main-sequence phase of solar mass stars.

7. X-RAY EMISSION AND OTHER STELLAR PROPERTIES

7.1. *Available Data*

In addition to the *R*-magnitudes measured by us for most sources from ESO/SERC plates, other stellar source parameters are available from the literature compilation and analysis by GS92. Details of the sample and computations are given in the notes to Table 6. They include measures of the internal energetics and structure of the star (bolometric stellar luminosity L_*, photospheric radius R_*, and effective temperature $T_{\rm eff}$), which may be related to convection and dynamo activity, and a fixed intrinsic star property (mass M_*). It should be stressed that the sample in Table 6 is biased toward well-studied optically selected T Tauri stars and lacks most of the X-ray–selected cloud members.

We also note that certain quantities in Table 6 are model-dependent. L_* and $L_{\rm disk}$ rely on the interpretation that the infrared excess is from a circumstellar accretion disk, although

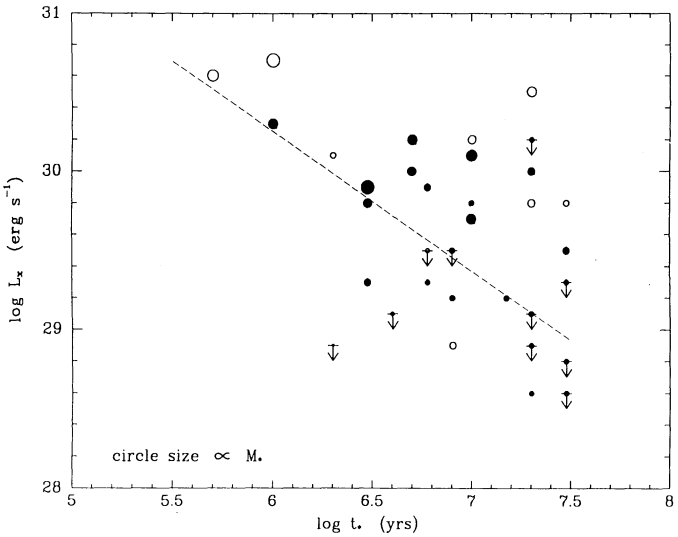

FIG. 7.—Correlation between X-ray luminosity L_X and stellar age for well-characterized cloud members. Filled (open) circles are CTT (WTT) stars, and the dashed line shows the linear regression computed using ASURV. The symbol sizes are proportional to stellar mass. Data for this and the following figures are given in Table 6.

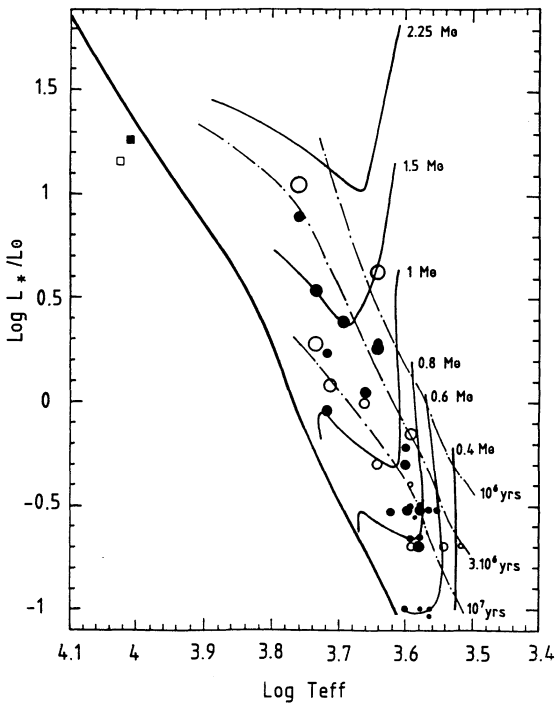

FIG. 8.—Hertzsprung-Russell diagram of well-studied T Tauri cloud members. Optical data and isochrones are from GS92 (Table 6). Filled (open) circles are CTT (WTT) stars, and the circle size is proportional to the X-ray luminosity, with undetected stars indicated by the smallest circle.

disk models are not always reliable, and cool unseen companions or starspots may be responsible for some infrared excess. M_* and t_* values are estimated from the theoretical isochrones used by GS92 (Vandenberg et al. 1983 for $M < 1\ M_\odot$ and Cohen & Kuhi 1979 for $M > 1\ M_\odot$), and different values would be found using the isochrones of other researchers. We have found, however, that the trends reported here are present when other isochrone models are adopted (e.g., Palla & Stahler 1993).

Figure 8 shows the Hertzsprung-Russell diagram of these well-characterized stars with the aim of summarizing links between X-ray and stellar properties. It is similar to the H-R diagram in GS92, except that the X-ray luminosity is reflected by the size of the open (WTT) or closed (CTT) circle for each star.

The results of the search for statistical relationships between X-ray emission are gathered in Table 7, with selected scatter plots shown in Figures 9–12. The table gives the star properties being compared, the number of detected and undetected stars examined (based on data in Table 6), and the probability that a correlation is *not* present. This last column gives the range of values found using three measures of correlation—Cox regression, generalizations of Kendall's τ, and Spearman's ρ—computed in the ASURV survival analysis software package. We delete the two well-known B9 stars HD 97048 and HD 97300, which have no outer convective zones, from the statistical analyses, though they are included in the figures (square symbols).

7.2. *X-Ray Emission versus Stellar Parameters*

A strong relationship between X-ray emission and stellar rotation is predicted by the dynamo model and is seen empirically in a wide variety of older late-type stars (e.g., Pallavicini et al. 1981). Projected rotational velocity, v sin i, measurements are available for only 16 well-characterized cloud members in the Chamaeleon I cloud (Franchini, Magazzu, & Stalio 1988; W92). The L_X–v sin i plot is shown in Figure 9. No correlation is found (Table 7); the stars scatter randomly around the $L_X \sim (v \sin i)^2$ relationship reported by Bouvier (1990), shown as the dot-dashed line. The scatter may be attributable to differences in the sin i projection factor and to X-ray variability. Choosing X-ray surface fluxes rather than total luminosities, or using the unprojected rotation periods available for four stars, does not improve the correlation.

While the data do not exhibit the expected activity-rotation relationship, they do show an unpredicted strong correlation

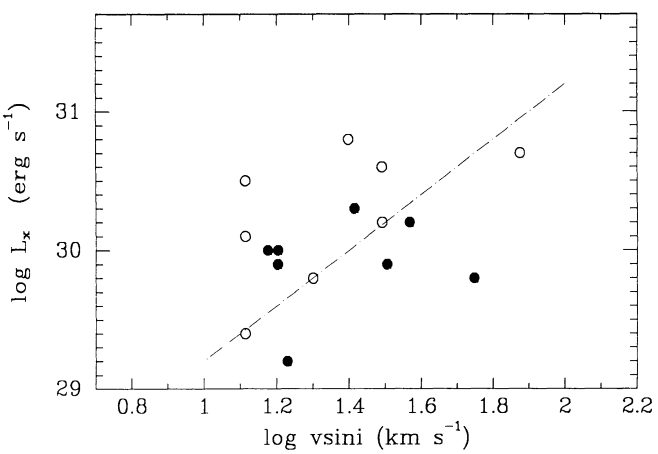

FIG. 9.—Plot of X-ray luminosity L_X vs. projected surface rotation velocity for 16 cloud members with measured v sin i. The line is the expected $L_X \sim (v \sin i)^2$ relation from Bouvier (1990).

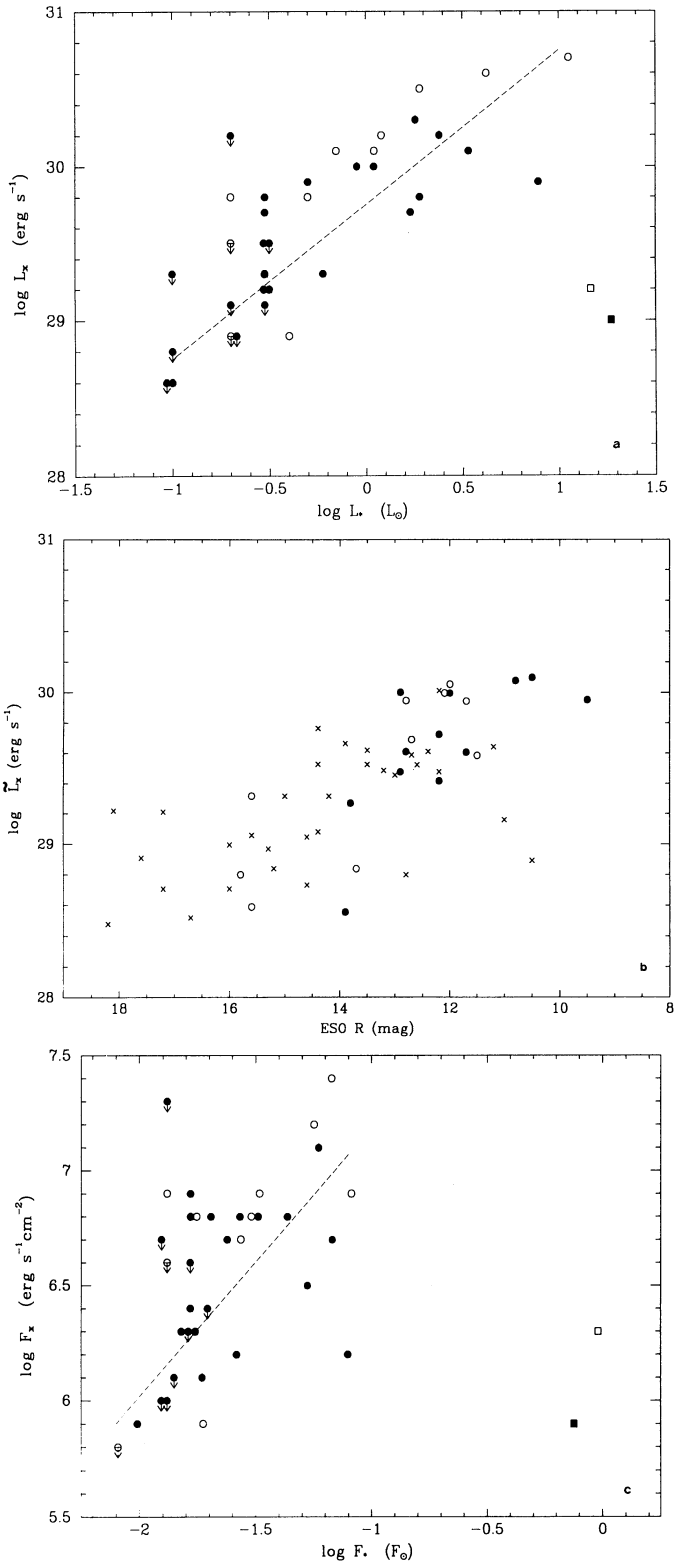

FIG. 10.—X-ray emission compared to bolometric stellar emission (with circumstellar infrared component removed). Filled (open) circles are CTT (WTT) stars, crosses are proposed New T Tauri stars, and squares are the two B9 stars. (*a*) Correlation between X-ray luminosity L_X and the stellar bolometric luminosity L_* (in $L_\odot$) for well-characterized cloud members. (*b*) Correlation between $\tilde{L}_X$ and *R*-band magnitude determined from MAMA photometry for all proposed *ROSAT* cloud members. (*c*) Correlation between X-ray flux F_X and the stellar bolometric flux F_* (in $F_\odot$) for well-characterized cloud members.

between L_X and the bolometric emission of the stellar surface L_* (Fig. 10*a*). Except for the two early-type stars having high volometric luminosities and low X-ray luminosities, the sample shows a clear power-law correlation. Using this modified sample, survival analysis regressions give the following the fit: $\log L_X(\text{ergs s}^{-1}) = 29.8\ (\pm 0.1) + 1.0\ (\pm 0.15) \log L_*/L_\odot$, with a residual scatter of only $\Delta(\log L_X) = 0.37$ standard deviation about the line.[7] CTT and WTT stars appear to follow this relationship equally. In other words, the X-ray luminosity of late-type Chamaeleon I stars is given by the simple proportionality $L_X/L_* = 1.6 \times 10^{-4}$ with a standard deviation of a factor ± 2.3. This relation is valid over two orders of magnitude, and the scatter may be largely due to X-ray variability and spectral differences.

The relationship between X-ray luminosity and stellar luminosity can also be examined for CTT, WTT, and New *ROSAT* stellar identifications having *R*-band magnitudes measured from our scan of the ESO/SERC plate (Appendix A). Figure 10*b* shows a rough correlation between the approximate luminosity $\tilde{L}_X$ and *R*. (A similar plot with only nine detections from *Einstein* X-ray images appears in FK89.) A tighter correlation might emerge if both *R*-magnitudes and $\tilde{L}_X$ values could be corrected for absorption effects, since the finding charts show that most of the fainter ($R > 15$) optical counterparts are deeply embedded in the cloud. In addition, the correlation in Figure 10*b* becomes stronger once two extreme points are removed: CHXR 8 and CHXR 11, two New sources with anomalously low $\tilde{L}_X$ and bright *R*, which unpublished spectroscopy indicates are early-type stars.

We note that Orion and Taurus-Auriga T Tauri stars observed in *Einstein Observatory* images have typical $L_X/L_* \simeq 3\text{–}10 \times 10^{-4}$ (Strom et al. 1990), $\sim$2–6 times higher than we find here. This difference may be the result of any combination of two effects: higher resolution of *ROSAT*, separating closely spaced T Tauri stars that are unresolved in *Einstein* images; and an age effect, described as follows. If we assume that a future order-of-magnitude increased sensitivity between *ROSAT* and *Einstein* for Orion pre–main-sequence stars will result in a decrease in mean X-ray luminosity similar to that seen for Chamaeleon (§ 6.2), the "*ROSAT*" mean log X-ray luminosity for the K stars of L 1641 will be about 30.7 ergs s^{-1} for an mean age $\langle t_* \rangle \sim 10^6$ yr. This value is one order of magnitude larger than the mean level we find in Chamaeleon where the average stellar age is $\sim 10^7$ yr, resulting in a factor of $\sim$2 decrease in the L_X/L_* ratio.

The linear scaling of X-ray with bolometric emission is reminiscent of that seen in early-type OB stars (Pallavicini et al. 1981: $L_X/L_{bol} \sim 10^{-7}$), where the emission is produced in hot, dense, high-velocity winds that are radiatively accelerated by the ultraviolet luminosity. However, the L_X/L_* ratio for OB stars is three to four orders of magnitude smaller than for T Tauri stars, illustrating that the X-ray emission mechanism is far more efficient in low-mass than in massive young stars.

We find that the L_X versus L_* correlation is also present, though with considerable scatter, when surface fluxes are considered. Figure 10*c* shows the X-ray surface flux F_X versus F_*,

[7] This regression fit was obtained with the EM algorithm under Gaussian assumptions and using Schmitt's (1985) binned regression method in the ASURV package. In this and other regression fits discussed below, the Buckley-James method gives a much steeper line with several fold larger residuals. We have ignored these poor fits, which are probably due to the concentration distribution of nondetections in the lower corner of the scatter plots.

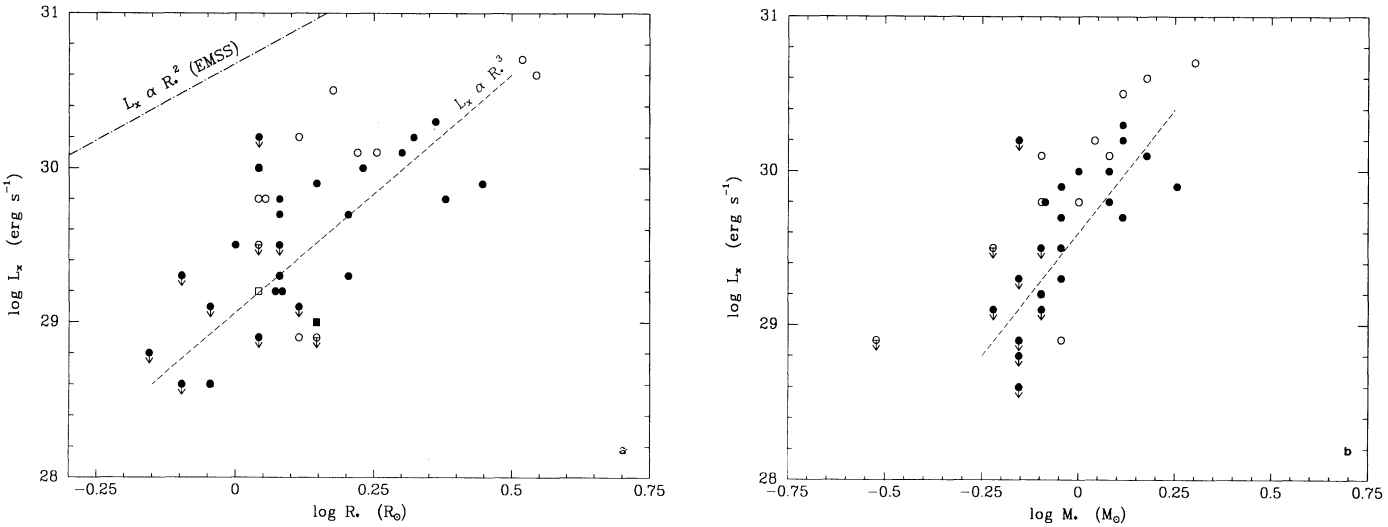

FIG. 11.—Correlation between the X-ray luminosity and other stellar properties. (*a*) Correlation between L_X and the stellar radius (in $R_\odot$). The line at the upper left is the saturation envelope of X-ray selected late-type main-sequence field stars detected in the *Einstein* Medium Sensitivity Survey (Fleming et al. 1989). (*b*) Correlation between L_X and the stellar mass (in $M_\odot$).

with a correlation present at the $P = 0.1\%$–0.3% confidence level. Combined with the stronger luminosity correlation, we tentatively infer that the X-ray–bolometric relationship is partly due to increased surface area available for magnetic structures, and partly to internal processes such as a dynamo mechanism.

Some researchers (e.g., Walter et al. 1988; Strom et al. 1990; GS92) have suggested that F_X may be approximately constant for pre–main-sequence stars due to a constant level of "saturation" of the dynamo effect in the stellar interior or of a magnetic heating process at the stellar surface. However, as shown in Figure 11*a*, the Chamaeleon I stars lie between 0.4 and 1.4 dex below the "saturation" line, defined by Fleming, Gioia, & Maccacaro (1989) as the empirical $L_X \propto R_*^2$ envelope for X-ray–selected late-type main-sequence field stars detected in the *Einstein* Medium Sensitivity Survey (EMSS). *Einstein* observations of L 1641 indicate that some of Orion pre–main-sequence stars do reach the "saturation" level (Strom et al. 1990). Compared to the L 1641 stars, however, our Chamaeleon I sample shows a similar range of R_* but with systematically lower L_X values. In addition, the Chamaeleon I stars show a steeper relation than in the "saturation" case, with $\log L_X = 29.0(\pm 0.1) + 3.0(\pm 0.4) \log R_*$. The X-ray surface flux thus appears to scale with the stellar radius. The actual regression fit is $\log F_X = 6.3(\pm 0.1) + 1.1(\pm 0.3) \log R_*$. In the magnetic activity model, this could arise if the X-ray emission scales primarily with the height of the magnetic loops confining the emitting plasma, as found in the case of strong X-ray flares (see Montmerle et al. 1993), and if this height itself scales with the stellar radius. Like the (F_X, F_*) plot, the (F_X, R_*) plot shows a large scatter, which may indicate that the size or emissivity of active regions differs for stars of the same bolo-

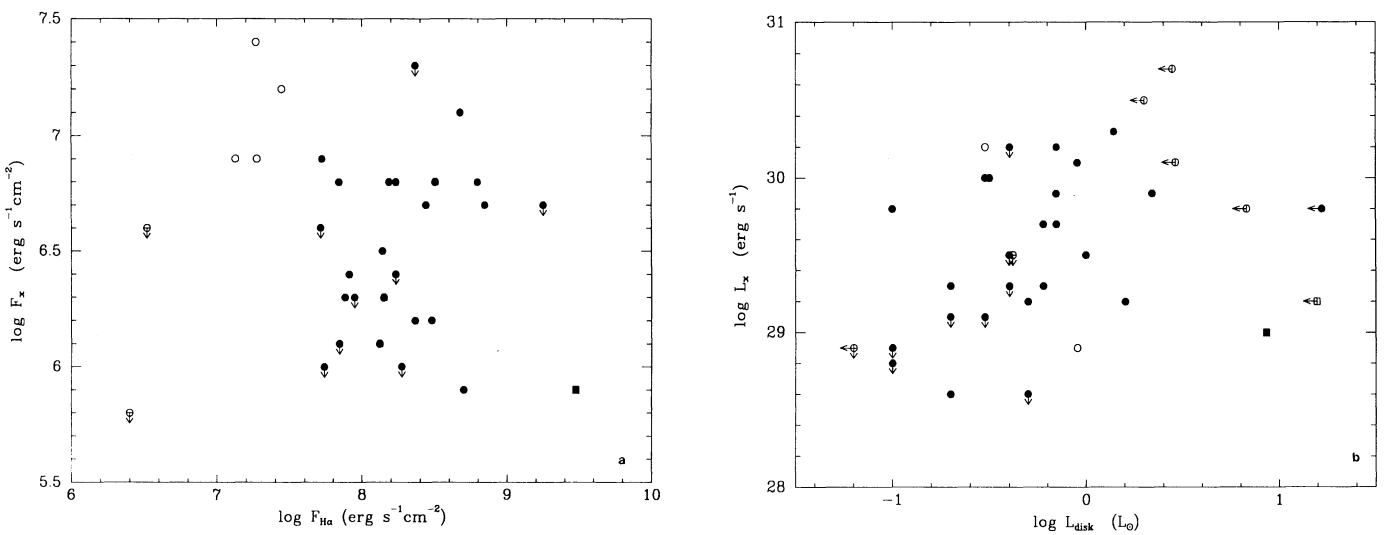

FIG. 12.—Correlation plots of X-ray emission vs. circumstellar properties of optically studied T Tauri stars. (*a*) F_X vs. the Hα surface flux. (*b*) L_X vs. the infrared luminosity of the circumstellar disk (in $L_\odot$) computed from GS92.

metric flux. Such a difference may be related to the stellar rotation velocity, or even to a time-variable phenomenon like activity cycles (e.g., Baliunas 1991).

Another notable finding is the strong correlation between L_X and M_* (Fig. 11*b*). Survival analysis linear regression fits give $\log L_X(\text{ergs s}^{-1}) = 29.6(\pm 0.1) + 3.6(\pm 0.6) \log M_*/M_\odot$ with a residual standard deviation of $\Delta(\log L_X) = 0.4$. The effect is also revealed by the symbol sizes in Figure 7, which are proportional to stellar mass. Higher mass stars consistently have higher X-ray luminosities than lower mass stars of the same age. Like the tight $L_X - L_*$ correlation, this relationship is not predicted by a simple magnetic activity model, but should be taken as a strong constraint on the actual mechanism. An interesting consequence of Figure 11*b* is that the horizontal scatter about the line is sufficiently small for stellar masses to be roughly predicted from X-ray observations. An X-ray luminosity function then corresponds to a mass function, allowing an estimation of the total stellar population of the Chamaeleon I cloud (§ 8.1).

Other relationships between X-ray luminosity or flux and bulk stellar parameters listed in Table 6 can be studied. Survival analysis statistical results given in Table 7 show that, in addition to mass and radius, L_X is strongly correlated with stellar effective temperature. It is not surprising that these correlations occur simultaneously, as $T_{\rm eff}$, M_*, R_*, and L_* are closely linked along the Hayashi tracks in the Hertzsprung-Russell diagram. The bottom half of Table 7 gives correlation results comparing F_X to these stellar properties. Except for the correlation $F_X \propto R_*$ discussed above, the dependencies are weaker than those seen with L_X, and most are no longer significant even though the total range of F_X is not significantly reduced from the range of L_X (the brightest stars are $10^{1.5}$–10^2 above the faintest stars in both variables.)

It is quite difficult with the present data to determine which variable(s) are causally linked to the X-ray emission. X-ray luminosity is strongly correlated with L_*, M_*, R_*, and $T_{\rm eff}$. None of these relationships are inherent in a simple dynamo mechanism, and may imply physical changes in dynamo efficiency as stars evolve along the Hayashi tracks. The most direct test of the dynamo model, comparison of L_X with $P_{\rm rot}$ or Rossby number (Noyes et al. 1984; Mangeney & Praderie 1984), cannot be performed until more stellar rotation data are obtained.

7.3. *X-Ray Emission versus Circumstellar Properties*

We examine here the optically selected T Tauri sample for possible effects associated with circumstellar material including winds/boundary layers, as traced by Hα, and circumstellar disks, as traced by the infrared luminosity $L_{\rm disk}$ computed by GS92. Early researchers suggested that ionized winds or accretion events in CTT stars (assumed to be traced by the Hα emission line) might be sufficiently hot to produce X-rays (Bisnovatyi-Kogan & Lamzin 1977; Mundt 1981), or sufficiently dense to absorb X-rays produced near the stellar surface (Walter & Kuhi 1981). *Einstein* studies showed no clear relation between Hα emission and X-ray emission in some (Montmerle et al. 1983; FK89) but not all (Walter & Kuhi 1981) studies.

In contrast to previous studies, we characterize here the Hα emission not by the equivalent width EW(Hα), but by the Hα surface flux F(Hα), which takes into account the spectral type and radius of the stars and has the same physical units as X-ray surface flux. Some Chamaeleon I stars have a considerable higher L_* than others, so that a low EW(Hα) does not necessarily mean that Hα emission is intrinsically weak. The F(Hα) fluxes are computed from the $L_{\rm H\alpha}$ luminosities tabulated in GS92. Table 7 and Figure 12*a* show the results for F_X versus F(Hα): there is no evidence for "smothering" of the X-rays by hot circumstellar material (probability of no correlation $> 50\%$), confirming previous analyses based on *Einstein* data.

Any role of a circumstellar accretion disk in producing or absorbing T Tauri X-rays may be studied by comparing X-ray luminosities and disk infrared luminosities. Figure 12*b* shows a scatter plot of $\log L_X$ versus $\log L_{\rm disk}$ from the data in Table 6.[8] A marginally significant correlation is found at a confidence level around 3% (Table 7). A linear regression fit using Schmitt's (1985) binned method gives a statistically insignificant slope, $\log L_X = 29.5(\pm 0.2) + 0.4(\pm 0.4) \log L_{\rm disk}$. It is not clear whether this association between L_X and $L_{\rm disk}$, if not a statistical artifact, is due to X-rays produced by the disk itself, or some indirect effect. For instance, in the case of standard optically thick viscous accretion, the disk luminosity is $L_{\rm disk} \propto M_* \dot{M}_{\rm acc}/R_*$, where $\dot{M}_{\rm acc}$ is the accretion rate. Alternatively, the $L_X - L_{\rm disk}$ association could be a by-product of stellar relationships (§ 7.2): L_* and $L_{\rm disk}$ are correlated in the GS92 sample, and L_X is strongly correlated with L_* (§ 7.2). Thus, a weak $L_X - L_{\rm disk}$ indirect correlation may be expected without a physical cause such as X-ray production in the disk.

Figure 12*b* also shows that some stars classified as WTT on the basis of their Hα emission alone turn out to be surrounded by luminous disks, and conversely that many CTT stars have low-luminosity disks, even when they have a large EW(Hα). This is another indication that caution must be exercised in the use of the WTT/CTT classification based on an Hα emission indicator, which is not obviously related to the amount of circumstellar material close to the star. Possible interpretations include holes or gaps in the inner disk region (e.g., Skrustskie et al. 1990; Montmerle et al. 1993; see also André & Montmerle 1993 for detailed discussion). It may also reflect poor fits to the disk model in some cases.

Despite the possible weak association between X-ray emission and the disk luminosity, these results are consistent with the standard view that X-rays emitted by optically selected T Tauri stars are stellar in nature, and are not significantly affected by the presence of winds, boundary layers, or disks.

8. STAR FORMATION IN THE CHAMAELEON I CLOUD

8.1. *The Pre–Main-Sequence Population*

Several recent studies (Gregorio-Hetem, Lépine, & Ortiz 1990; GS92; P92) have investigated the bolometric luminosity function of Chamaeleon I cloud members, based on 56–58 optically selected T Tauri stars and 10–20 infrared selected embedded stars. This study suggests that the pre–main-sequence population of the cloud is considerably larger than this. Our *ROSAT* images directly show 19 (strong Reliability 1) to 39 (Reliability 1 + 2) "New" identifications, most of which are probable new WTT stars (§ 4).

[8] Since $L_{\rm disk}$ is calculated from the near-infrared excess, this quantity traces only the inner regions of the disk ($\lesssim 1$ AU; Strom et al. 1990), which is probably only $\sim 1\%$ of the total disk radius. The outer, colder regions have to be probed with sensitive far-infrared to millimeter measurements, which have not yet been obtained for Chamaeleon low-mass stars.

The presence of even more WTT stars can be inferred for a number of reasons: WTT stars may exist with X-ray luminosities below the present *ROSAT* sensitivity limit; WTT stars should be present on the far side of the cloud, which are obscured at optical and X-ray wavelength and have no infrared excesses; and a number of WTT stars may possibly be embedded deep in the cloud cores, similar to those found in the ρ Oph cloud via their nonthermal centimeter radio emission (Leous et al. 1991). If the far side of the cloud is similar to the near side, and if the ratio of WTT to CTT stars embedded in the cloud core is as high as in the visible portions, then several dozen embedded WTT stars remain to be discovered. Altogether, we estimate that the total cloud population of low-mass pre–main-sequence stars may be as high as 200 cloud members.

The total T Tauri population can also be inferred from the observed X-ray luminosity function (§ 5) combined with the $L_X - M_*$ correlation (§ 7.2) to give a mass function for PMS stars in the cloud. (We note here that this is not the classical "initial" mass function [IMF], since in this case "initial" means on the ZAMS.) From Figure 6*b*, the X-ray luminosity function of all X-ray–emitting stars can be approximated by $N(> \log \tilde{L}_X) = -54.1\ (\pm 0.7) \times (\log \tilde{L}_X - 30.18 \pm 0.04)$. We assume $\tilde{L}_X \simeq L_X$ and impose a mass function of the form $d(N_*)/d(\log M_*) = AM_*^{\alpha}$ similar to the classical IMF. We then find from Figure 11*b* for the mass range $0.5 \lesssim M_*/M_\odot \lesssim 2$: $\log L_X = 29.7 \times M_*^{0.05}$, or $A = -80$, $\alpha = 0.05$. Note the slightly increasing value of this index, compared with the decreasing value $\alpha \approx -1.4$ usually found for the classical IMF. Integrating between 0.5 and 2 $M_\odot$ gives a total of 110 stars (20 more than the total number of detected stellar X-ray sources), having a combined mass of 120 $M_\odot$. If we extend this mass function to stars with $0.1 \lesssim M_*/M_\odot < 0.5$, most of which would have X-ray luminosities below the current *ROSAT* sensitivity limit, we predict 230 stars with a combined mass of 150 $M_\odot$.

In principle, one can use these estimates of the pre–main-sequence stellar population to estimate the star formation efficiency, defined as the ratio of stellar to (stellar + present gas) mass in the cloud. However, the molecular and neutral gas of the Chamaeleon I cloud has not been adequately studied on the scales of interest for an accurate measurement. Dame et al. (1987) report a gas mass of 5000 $M_\odot$ from CO ($J = 1 \rightarrow 0$) observations over 8 deg^2. Mattila, Liljeström, & Toriseva (1989) reported a gas mass of 450 $M_\odot$ from various CO isotope measurements in $\sim$0.5 deg^2 around the southern cloud cores. The total gas mass within the $\sim$4 deg^2 containing most of the WTT and CTT stars lies somewhere between these extreme values. If one considers only the dense cloud cores, and assumes the north core also has a mass around 250 $M_\odot$ like each of the southern cores, then the star formation efficiency is about 150 $M_\odot$/(450 + 250 $M_\odot$) $\simeq$ 20%.

8.2. *A Star Formation Scenario for Chamaeleon*

We can attempt to combine the Chamaeleon I stellar population (§§ 5, 8.1), spatial (§ 4.3), and age (§ 6.2) distributions into a simple star formation scenario. The dense cloud cores (or, if they are short-lived, similar cores in the past) produce both CTT and WTT stars at a constant rate over an extended period of time, at least $\sim 3 \times 10^7$ yr (the oldest t_* in Table 6). Initially, the ratio of WTT to CTT stars is perhaps 1:1, as seen at the uppermost portion of the Chamaeleon I Hertzsprung-Russell diagram (Fig. 8, plus a few luminous New stars). Integrated over 1×10^7 yr or longer, $\gtrsim$20% of the gas in the cloud cores is converted into stars.

As the CTT stars age, their circumstellar disks cease interacting with the stellar surfaces converted them from CTT to WTT stars. The CTT/WTT transition epoch may vary between $\sim$several 10^5 and $\sim$several 10^7 yr (note that several CTT stars in Table 6 have $t_* > 1 \times 10^7$ yr; see Strom et al. 1989 and Montmerle & André 1989 for discussions of this transition). Simultaneously, the stars drift outward at speeds of $\sim$0.1 km s^{-1}. The result should be a radially symmetric distribution of X-ray–emitting PMS stars extending several parsecs around the cloud cores with the WTT:CTT ratio increasing to $\gtrsim$3:1 far from the cores. This increase must take place at distances $\gtrsim 1°$ from these cores, since we see no variation of this ratio within our images. However, older WTT stars are probably present in our fields but still undetected either because their X-ray emission, which averages around several 10^{29} ergs s^{-1} during the first 10^7 yr, falls below the *ROSAT* sensitivity limit of several $\times 10^{28}$ ergs s^{-1} after several 10^7 yr, or because they have intrinsically weaker X-ray emission as is the case for half of the optically selected T Tauri stars (Table 6). This scenario also predicts perhaps 20–40 more yet-undetected X-ray–emitting stars embedded near the cloud cores associated with the infrared-excess stars in the cores. Both the young core CTT + WTT and older periphery WTT stars should be discoverable with forthcoming telescopes sensitive to hard X-rays.

Finally, it is interesting to compare the Chamaeleon I cloud to the star-forming cloud cores within the Orion giant molecular cloud L 1530 studied by Lada (1992). The Orion cloud cores NGC 2068 and 2071, for example, have diameters of 1–2 pc, 300–500 $M_\odot$ of dense (10^4 cm^{-3}) molecular gas, and 100–200 young stars with $L_{bol} > 0.2\ L_\odot$. The Chamaeleon I cloud has a diameter of 2–5 pc, $\sim$700 $M_\odot$ of dense gas (our estimate from Mattila et al. 1989), and an estimated 200 young stars of mass $> 0.1\ M_\odot$. These similarities suggest that star formation within giant molecular clouds like Orion, and within more isolated small molecular clouds like Chamaeleon I, share many characteristics.

9. SUMMARY

We have used the *ROSAT* satellite to survey the X-ray emission from PMS stars in the whole Chamaeleon I cloud, with two overlapping exposures. We review here the principal findings with implications for X-ray astronomy, stellar activity, and star formation. Readers interested in specific Chamaeleon I T Tauri stars should consult the detailed tables, finding charts, and Appendix B. All luminosities are based on an assumed cloud distance of 140 pc, and the distinction between "classical" and "weak" T Tauri (CTT and WTT) stars is here based solely on the stellar Hα emission-line equivalent width (> 10 Å and < 10 Å, respectively) or intensity.

1. Modern X-ray telescopes and detectors give a major boost to observational studies of low-mass pre–main-sequence stars. The modest 6 ks exposures with the *ROSAT* PSPC described here detects 71 certain or probable T Tauri stars, comparable to the number found in several decades of Hα and infrared surveys. Accurate boresight and narrow point-spread functions, giving 4″ on-axis X-ray error circle radii, are crucial to the reliable identification of X-ray sources with CTT and

WTT stars (§§ 2–3). No Herbig-Haro objects were detected in X-rays. One source (CHXR 49) appears extended, but may consist of two or three incompletely resolved stars (§ 3).

2. These *ROSAT* X-ray images, sensitive to about $\tilde{L}_X = 6 \times 10^{28}$ ergs s^{-1} in the inner regions of the PSPC ($<20'$), detect 34 out of 60 previously known T Tauri stars. They also point to 19–39 probable "New" cloud members. Some are embedded in the cloud with $15 < R < 19$, but most are bright and relatively unobscured with $11 < R < 15$. We predict optical spectroscopy will show that most of these "New" stars are WTT stars (§§ 3, 4.2).

3. X-ray–detected WTT stars plus proposed New cloud members outnumber CTT stars in the Chamaeleon I by about 3:1. These *ROSAT* images directly increase the cloud membership by 35%–60%. Estimates of the total pre–main-sequence stellar population, including stars embedded within and on the far side of the cloud, are ~ 200 stars (§§ 4.1, 8). X-ray telescopes like *ASCA*, *AXAF*, and *XMM*, which can image at higher energies where interstellar absorption is reduced will probably detect significant numbers of deeply embedded pre–main-sequence stars.

4. Little difference is found in the systematic properties of Chamaeleon I CTT, WTT, and New stars. The CTT and WTT stars have virtually identical spatial distributions around the cloud (§ 4.3), and (where optical data are available) locations in the Hertzsprung-Russell diagram (Fig. 8). WTT stars have a somewhat stronger X-ray luminosity distribution, but this difference may disappear when the proposed New stars are characterized (§ 5).

5. The conditions peculiar to CTT stars—winds, disks, and boundary layers—do not produce the observed X-ray emission. We find no evidence for a relationship to Hα emission. Various arguments support the interpretation that solar-type magnetic activity is responsible for both CTT and WTT X-ray emission (Feigelson et al. 1991; Montmerle et al. 1993).

6. The approximate X-ray luminosities of low-mass pre–main-sequence stars range from $\log \tilde{L}_X < 28.8$ to 31.2 ergs s^{-1}. The mean $\langle \log \tilde{L}_X \rangle = 29.2$ ergs s^{-1} for an unbiased optically selected sample (§ 5). This is significantly higher than the mean X-ray luminosity in young main-sequence stars, found with *Einstein*, and there is some evidence for temporal decrease of X-ray emission along the Hayashi track (§ 7). The mean luminosities are found to be lower (by a factor $\simeq 2.3$) with respect to *Einstein Observatory* studies, as a result of the improved angular resolution and sensitivity of *ROSAT*.

7. The X-ray luminosities of well-studied Chamaeleon I cloud members are uncorrelated with $v \sin i$ but are strongly correlated with a complex of four interrelated stellar properties: bolometric luminosity, effective temperature, mass, and radius (§ 7.2). The $L_X - L_{bol}$ relation can be expressed by the simple statement that low-mass Chamaeleon I stars have $L_X/L_* = 1.6 \times 10^{-4}$, with a scatter of a factor of ± 2.3. The surface flux does not appear to be saturated and is found to be proportional to the stellar radius. These relationships are not well understood; the scalings between X-ray and bolometric stellar luminosities and masses are *not* directly predicted by the dynamo magnetic activity model. They should be a strong constraint on the actual mechanism.

8. A scenario for star formation in the Chamaeleon I cloud is suggested that describes the population, spatial, and age distributions of its pre–main-sequence stars. It involves the initial production of comparable numbers of CTT and WTT stars, the conversion of the CTT into WTT stars on time scales of 10^5–10^7 yr, and the undetectability of X-ray emission on time scales $\gtrsim 10^7$ yr. Based on the total T Tauri population, the star formation efficiency of the cloud is estimated to be $\gtrsim 20\%$.

We would like to thank Jeff Mendenhall for his expert assistance with data analysis, David Burrows for making available a third *ROSAT* image, Sylvie Cabrit and Jane Gregorio-Hetem for useful discussions, Robert Stern, and the referee Fred Walter for helpful comments. S. C. thanks the Department of Astronomy & Astrophysics at Penn State for hospitality in the course of this work. This study benefited from the SIMBAD database operated by Centre des Données Stellaires (CDS) in Strasbourg, and the NASA Astrophysics Data System. The work was partially supported by NASA grants NAG 5-1678 and NAGW-2120.

Note added in manuscript.—A number of the proposed "New" cloud members from the *ROSAT* source lists have recently been found to have T Tauri optical spectra. A deep objective prism survey for Hα emitting stars by Hartigan (1993) shows eight coincidences with "New" *ROSAT* sources: CHXR 12 = Hn 3, CHXR 21 = Hn 6, CHXR 35 = Hn 35, CHXR60 = Hn 18 or 19, CHXR 62 = Hn 20, CHXR 71 = Hn 1, CHXR 79 = Hn 9, and CHXR 84 = Hn 16. Optical spectroscopy by Huenemoerder, Lawson, & Feigelson (1993) shows a number of stellar counterparts of "New" sources have strong Li 6707 Å absorption and weak Hα emission characteristic of WTT stars. These include CHXR 35, 37, 40, 47, 59, and 68.

APPENDIX A

STELLAR COUNTERPARTS ON THE ESO/SERC SKY SURVEY

The Chamaeleon I cloud lies in field 38 of the ESO/SERC Southern Sky Survey. Portions of the red plate around *ROSAT* sources, astrometric and photometric standards were digitized with 10 μm (0.″65) pixels on the MAMA (Machine Automatique à Mesurer pour l'Astronomie) high-speed microdensitometer at the Centre d'Analyse des Images[9] located at the Observatoire de Paris. The instrument, reduction system, calibration, digitization procedures, and object detection procedures are described by Berger et al. (1991). Cubic polynomial two-dimensional plate solutions were constructed using 90 reference stars (with positions corrected for proper motion, accurate to 0.″34 in R.A., and 0.″36 in decl.) between $J = 6$ and 10, from the PPM astrometric catalog (Röser & Bastian 1991). The resulting solution has an internal standard deviation of $\pm 0.''45$ for a given reference star.

[9] MAMA is operated by INSU (Institut National des Sciences de l'Univers).

TABLE 8

MAMA POSITIONS FOR PROPOSED STELLAR COUNTERPARTS OF *ROSAT* SOURCES IN THE CHAMAELEON I CLOUD

CHXR	α	δ	CHXR	α	δ	CHXR	α	δ
1	10 56 30.9	-77 11 39.2	31	11 08 01.6	-77 42 28.6	61	11 13 33.6	-76 35 37.1
2	...	...	32	11 08 15.2	-77 33 52.7	62	11 14 15.8	-76 27 36.4
3	10 58 05.5	-77 28 23.6	33	11 08 40.8	-76 36 07.6	63	...	...
4	...	...	34	...	...	64	...	...
5	10 59 01.1	-77 22 40.9	35	...	...	65	11 16 13.1	-77 13 06.8
6	10 59 07.0	-77 -1 40.1	36	11 09 12.2	-77 29 12.1	66	11 17 37.1	-77 04 38.0
7	10 59 25.8	-77 37 57.5	37	11 09 17.8	-76 27 57.7	67	...	...
8	11 00 14.7	-77 14 38.0	38	11 09 18.0	-77 47 39.8	68	11 18 20.2	-76 21 58.5
9	11 01 18.2	-76 26 59.2	39	11 09 23.6	-76 23 21.8	69	...	...
10	11 02 25.0	-77 33 35.5	40	11 09 40.1	-76 28 39.9	70	...	...
11	11 03 11.7	-77 21 10.7	41	11 09 54.2	-76 29 25.4	71	11 02 32.7	-77 29 12.7
12	11 03 57.0	-77 21 32.9	42	...	...	72	11 04 11.2	-76 54 32.1
13	...	...	43	11 09 58.8	-77 37 08.9	73	11 06 28.9	-77 37 33.0
14	...	...	44	...	...	74	11 06 57.4	-77 42 10.4
15	11 05 43.1	-77 26 51.7	45	...	...	75	11 07 08.9	-76 32 27.3
16	11 05 57.6	-76 07 49.1	46	11 10 07.3	-76 29 38.6	76	11 07 35.3	-77 34 49.1
17	11 05 50.6	-77 07 22.5	47	11 10 38.1	-77 32 39.7	77	...	...
18	11 05 52.7	-76 18 25.4	48	...	...	78	...	...
19	11 06 16.3	-77 22 17.2	49	...	...	79	11 09 18.2	-76 30 29.2
20	11 06 45.2	-77 27 01.9	50	...	...	80	...	...
21	11 07 11.6	-77 46 39.1	51	11 12 27.8	-76 44 24.7	81	...	...
22	11 07 13.4	-77 43 49.5	52	...	...	82	11 10 53.5	-76 34 31.9
23	11 07 20.8	-77 38 03.3	53	11 12 28.1	-76 25 29.4	83	...	...
24	11 07 28.4	-76 52 11.8	54	11 12 42.2	-76 58 40.0	84	...	...
25	11 07 33.4	-77 28 28.1	55	11 12 43.5	-76 37 06.0	85	11 12 10.0	-76 34 36.3
26	11 07 37.1	-77 33 32.9	56	11 12 42,6	-77 22 25.5	86	...	...
27	...	...	57	11 13 20.3	-77 01 04.2	87	...	...
28	11 07 56.0	-77 27 25.2	58	...	...	88	...	...
29	...	...	59	11 13 27.6	-76 34 16.3	89	...	...
30	11 08 00.1	-77 17 30.6	60	11 13 29.8	-76 29 01.2			

We have compared MAMA star positions with those given in the GSC for all stars listed in column (6) of Table 4. MAMA positions are found to be systematically $1''.6 \pm 0''.1$ west of GSC positions, with a standard deviation of $\pm 1''.4$ about this systematic offset. The offset occurs in all four GSC Schmidt plates used in the Chamaeleon I region. We believe these offsets and dispersions are due primarily to errors in the Guide Star Catalog positions. At these extreme southern declinations, GSC positions are based on the first Cape Photographic Catalog (Stoy 1986) and the FK3 system and were not corrected to the SAO catalog or later FK systems. GSC plate solutions based on the CPC catalog have $0''.94$ standard deviation when reduced against the AGK3 catalog (Russell et al. 1990). Russell et al. do not have an estimate of the external error of the GSC-CPC positions, which might account for the systematic offset we find here. We note only that the GSC external errors appear to be higher in the southern hemisphere, with standard deviation of $1''.2$ at $\delta = -25°$ and $-35°$. Given these known deficiencies in the extreme southern GSC positions, and the fact that MAMA positions are based on the high-quality PPM system, the MAMA positions are probably more accurate than those in the GSC. To assist future study of these stars, we provide in Table 8 MAMA positions for proposed identifications listed in Table 4. Positions for sources affected by nebulosity, with ambiguous identification, or otherwise unavailable, are omitted.

Photometric standards of 30 nonvariable stars between $R = 6.4$ and 13.7 from the photometry by Whittet et al. (1987) were scanned with MAMA to construct a calibration between MAMA scan intensities and R-magnitude. Because many *ROSAT* counterparts are fainter than $R = 13.7$, and no deeper photometric sequence is available near the cloud, we also scanned ESO/R plate 324 containing 18 CCD photometric standards between $R = 9.6$ and 19.7 from Graham (1981; Table 1) and Zickgraf et al. (1990; Table 3 stars 1–11). A small offset equivalent to 0.1 mag was necessary to align the two sequences, due to differences in the ESO plates and/or MAMA settings. A nonlinear relation between the MAMA intensities and R-magnitudes was fitted by eye to the combined photometric sequence. In the $R = 11$–14 interval where the density of standards is sufficient to estimate the scatter, a standard deviation of $\Delta R \sim 0.15$ is found. This calibration curve was then used to convert MAMA intensities to R-magnitude for the proposed *ROSAT* stellar counterparts; results are given in column (5) of Table 4. As in Table 8, some entries are omitted. A reasonable estimate of the total uncertainty of these magnitudes is ± 0.3 (90% confidence level).

APPENDIX B

NOTES ON THE FINDING CHARTS AND STELLAR IDENTIFICATIONS

Except where noted, all positions and other properties of previously known CTT and WTT stars are obtained from GS92. The list is ordered by CHXR number.

2. A prominent star lies just off the NW edge of the finding chart and is a possible stellar identification.
3. Offset and magnitude are given for the bright star to the N.

4. The WTT star SZ Cha is the bright star to the W slightly outside the X-ray error circle. However, as the X-ray positional error is uncertain far off-axis, the bright star to the E is also a plausible counterpart. We have selected SZ Cha as the identification, with Reliability Class 2. Two faint infrared companions 5″ and 12″ from SZ Cha are present (Chen & Graham 1992).

7. Offset and magnitude are given for the brighter star to the N.

9. Several stars lie within the large X-ray error circle. GSC 9410−2542 is the middle and brightest of the three stars NE of the *ROSAT* position. It appears to be a visual double.

13. CT Cha is the brightest star SW of the *ROSAT* centroid. The finding chart for this source was made separately from the others; it is deeper and has a different gray-scale transfer function compared to the other charts. It has an infrared companion 2.″5 to the east (Chen & Graham 1992).

14. One or both of the two bright stars E of the field center are likely stellar counterparts.

16. SAO 256798, B6 IV-V. Whittet et al. (1987) place this star behind the cloud, assuming a cloud distance of 140 pc, but membership is possible if the cloud lies around 200 pc. Accurate radial velocity measurement could resolve this question. We have tentatively classified the star as "*U*", probably unrelated to the star forming cloud.

17. The star just NW of the *ROSAT* centroid (CHX 6a) is a M0 BY Draconis–type spectroscopic binary without Li 6707 Å absorption, lying in front of the cloud. It is the probable X-ray emitter. The star further to the NW (CHX 6b) is an ordinary M0 III star (W92).

19. The Guide Star Catalog lists this star as both GSC 9414−0787 and GSC 9414−1052 separated by 19″, with inaccurate positions. It is apparently confused by the bright nebulosity.

20. The star 26″ to the N is the WTT star UX Cha, which was (incorrectly) suggested by FK89 as the counterpart to CHX 8. UX Cha is also incorrectly labeled in FK89's finding chart.

22. The *ROSAT* error circle is consistent with both of these faint stars.

23. In the list of S92, this star is designated CoD −76°486. It may have up to three infrared companions within 1″ (Chen & Graham 1992).

24. May be a close binary with $<1''$ separation (Chen & Graham 1992).

27. This CTT star 17″ to the W lies outside the 8″ X-ray error radius. But the X-ray photons are not tightly grouped, and the SASS maximum-likelihood algorithm may have overestimated the accuracy of the position. The bright star to the E is HD 97048 (see CHXR 29).

28. This star, CHX 10a, is a confirmed WTT cloud member (W92).

29. Like nearby CHXR 27, this source is poorly located, and its association with the bright Herbig Ae/Be star HD 97048 is uncertain. Note that the position of this star is inaccurate in the SIMBAD and GSC catalogs due to nebulosity.

30. CHXR 30 lies within 7″ of *IRAS* source F11065−7701 = B38 (Baud et al. 1984), and is associated with a faint optical star in a highly obscured portion of the cloud. The infrared flux densities are 0.31 Jy (12 μm band), 0.39 Jy (25 μm), and <0.35 Jy (60 μm, 95% confidence).

32. The reliability class is 2 because it is not clear which component of the visual binary (FK89) is the X-ray emitter. P92 indicates only one component has a near-infrared excess. We adopt the WTT classification of GS92; however, recent observations show Glass I is a WTT/CTT binary (Gregorio-Hetem et al. 1992).

33. This M0e star was examined by FK89 as a counterpart to an *Einstein* X-ray source. Since its membership in the cloud has not been confirmed from lithium line or radial velocity measurements, we classify it as "New" here.

34. The bright star 45″ to the S is the GSC star. It lies outside the nominal 30″ radius X-ray error circle, but we consider the identification to be plausible since the source is weak and very far off-axis.

35. This weak source is located close to the stronger CHXR 37; its centroid and error radius were estimated by visual inspection and may not be accurate. Two possible faint optical counterparts are seen in the finding chart and are located 18″ from the embedded infrared source C1–15 (Hyland, Jones, & Mitchell 1982).

36. The reliability class is 2 because it is not clear which component of the visual binary is the X-ray emitter.

38. SAO 256804 = HD 97240, F5 V. Main-sequence F stars are frequent serendipitous sources in soft X-ray surveys (e.g., Schmitt et al. 1985).

40. This M1e star was examined by FK89 as a counterpart to an *Einstein* X-ray source. Since its membership in the cloud has not been confirmed from lithium line or radial velocity measurements, we classify it as "New" here. The bright star to the SE is an ordinary A7 star (FK89).

41. The bright star lying at the NW is an ordinary A7 star (FK89); see note for CHXR 40. Sz 33 may be a close binary with $<1''$ separation (Chen & Graham 1992).

47. This source lies within 4″ of *IRAS* source F11091−7716 (which could be the embedded star C7-11; Hyland et al. 1982) and is coincident with a moderately bright optical star in an obscured cloud region. Its infrared flux densities are 0.28 Jy (12 μm band), 0.41 (25 μm band), and 0.28: (60 μm band).

49. The finding chart is centered on the nominal *ROSAT* centroid, although the X-ray source is extended (see note to Table 2). The X-ray–brighter NE portion of the source could be due to the star 24″ NE of the chart center near the edge of optical nebulosity. This star has not been cataloged or studied. The X-ray–fainter SW portion could be due to CHX 18N, which is a WTT cloud member (W92). CHX 18N also appears to be the source of the *IRAS* source F11101−7603, whose infrared position is about 7″ from the optical star. The CTT XX Cha 42″ SW of the chart center may also contribute to the edge of the X-ray structure. The brightest star in the chart, 46″ S of the chart center, is CHX 18S and is unrelated to the cloud.

50. The X-ray location lies between two bright stars separated by 11″, somewhat closer to the SW WTT star Sz 41. The NE star, GSC 9410−0800 = CHX 20a, is a K0 III star with radial velocity and Li 6707 Å inconsistent with cloud membership (W92). We therefore consider the identification with Sz 41 to be reliable.

51. The X-ray location lies directly on the bright CTT star LkHα 332–21, and 12″ W of the CTT star HM 31. Since the *ROSAT* error circle is very small (the SASS maximum-likelihood uncertainty is only 1.″5) the identification with LkHα 332–21 seems reliable. An infrared companion 1.″8 south of the star is present (Chen & Graham 1992).

52. Both of the two stars near the finding chart center are consistent with the X-ray position.

53. Despite the crowded optical field, the identification with the star at the finding chart center seems reliable due to the small X-ray error circle.

54. The bright star NE of the chart center is CHX 21a, a confirmed WTT cloud member (W92).

55. The bright star at the chart center is CHX 20E, a confirmed WTT cloud member (W92).

58. This source may be of extragalactic origin.

60. The NE star lies 11″ and the SW star lies 18″ from the X-ray position, both outside the SASS 6″ radius error circle. The NE star is the more likely identification, but with low reliability.

63. This is a weak off-axis source not found by the SASS processing and with no clear optical counterpart. The source may be spurious.

64. A nearby ($z = 0.0059$) 15.9 mag barred (SBab peculiar) spiral galaxy detected with *IRAS*. For $H_0 = 75$ km s^{-1} Mpc^{-1}, the soft X-ray luminosity is 2×10^{40} ergs s^{-1}, typical of a spiral with active star formation.

66. The CTT star HM 32 is nearest the chart center and is the likely identification, but the X-ray error circle does not exclude the two stars to the E.

68. We suggest the bright visual binary 20″ to the NW as a tentative identification, although the X-ray error circle also includes other fainter stars.

69. This bright star 47″ SW of the X-ray centroid is the likely identification for this strong off-axis source. It is uncataloged and unstudied to date.

70. Due to the uncertain X-ray error circle far off-axis, identification of this very bright X-ray source with the star HD 99558 (K0 III) 64″ to the NE is possible. However, an extragalactic origin is also plausible.

71. This star lies 4″ outside of the SASS maximum-likelihood error circle, but is probably a reliable identification.

74. This embedded star lies 10″ E of the *ROSAT* centroid, just outside the SASS error circle.

75. The prominent WTT star Sz 17 lies 15″ NW of the *ROSAT* centroid, outside the SASS error circle.

77. The star to the SW lies 47″ from the *ROSAT* centroid. As this is far outside the SASS error circle, we list this identification as unknown.

78. Either the faint central embedded star, or the brighter star 20″ to the N, is the likely identification.

79. This location lies 10″ from the embedded infrared source C1–18 (Hyland et al. 1982).

84. This source has a likely faint optical counterpart, but it is unclear whether it is stellar or extragalactic.

REFERENCES

André, P., & Montmerle, T. 1993, ApJ, submitted
Balinuas, S. 1991, in The Sun in Time, ed. C. P. Sonnett et al. (Tucson: Univ. Arizona Press), 809
Baud, B., et al. 1984, ApJ, 278, L53
Berger, J., Cordoni, J. P., Fringant, A. M., Guibert, J., Moreau, O., Reboul, H., & Vanderriest, C. 1991, A&AS, 87, 389
Bertout, C. 1989, ARA&A, 27, 351
Bisnovatyi-Kogan, G. S., & Lamzin, S. A. 1977, Soviet Astron., 21, 720
Bouvier, J. 1990, AJ, 99, 946
Caillault, J.-P., & Zoonematkermani, S. 1989, ApJ, 338, L57
Casanova, S., et al. 1993, in preparation
Chen, W. P., & Graham, J. A. 1992, in Complementary Approaches to Double and Multiple Star Research, ed. H. McAlister & W. I. Hartskopf (San Francisco: ASP), 60
Cohen, M., & Kuhi, L. V. 1979, ApJS, 41, 743
Dame, T. M., et al. 1987, ApJ, 322, 706
Damiani, F., Micela, G., & Vaiana, G. S. 1991, in Angular Momentum Evolution of Young Stars, ed. S. Catalano & J. R. Stauffer (Dordrecht: Kluwer), 89
Daniel, W. W. 1989, Applied Nonparametric Statistics (Boston: PWS-Kent)
Davies, J. K., Evans, A., Bode, M. F., Whittet, D. C., & Kilkenny, D. 1991, MNRAS, 252, 271
Feigelson, E. D., Giampapa, M. S., & Vrba, F. J. 1991, in The Sun in Time, ed. C. P. Sonnett et al. (Tucson: Univ. Arizona Press), 658
Feigelson, E. D., Jackson, J. M., Mathieu, R. D., Myers, P. C., & Walter, F. M. 1987, AJ, 94, 1251
Feigelson, E. D., & Kriss, G. A. 1989, ApJ, 338, 262 (FK89)
Feigelson, E. D., & Nelson, P. I. 1985, ApJ, 293, 192
Fleming, T. A., Gioia, I. M., & Maccacaro, T. 1989, ApJ, 340, 1011
Franchini, M., Magazzu, A., & Stalio, R. 1988, A&A, 189, 132; erratum A&A, 197, 354
Franco, G. A. 1991, A&A, 251, 581
Gauvin, L. S., & Strom, K. M. 1992, ApJ, 385, 217 (GS92)
Graham, J. A. 1981, PASP, 93, 291
Gregorio-Hetem, J. C., Lépine, J. R., & Ortiz, R. P. 1990, Rev. Mexicana Astron. Af., 21, 356
Gregorio-Hetem, J. C., Lépine, J. R., Quast, G. R., Torres, C. A. O., & de la Reza, R. 1992, AJ, 103, 549
Hartigan, P. 1993, AJ, 105, 1511
Hoffmeister, D. 1963, Veroff. Stern. Sonneberg, 6, No. 1
Hohenberg, C. M., Nichols, R. H., Olinger, C. T., & Goswami, J. N. 1990, Geochim. Cosmochim. Acta, 54, 2133
Huenemoerder, D., Lawson, W., & Feigelson, E. 1993, in preparation
Hyland, A. R., Jones, T. J., & Mitchell, R. M. 1982, MNRAS, 201, 1095
Isobe, T., Feigelson, E. D., & Nelson, P. I. 1986, ApJ, 306, 490
Koch, G. G., Sen, P. K., & Amara, I. 1982, in Encyclopedia of Statistical Sciences, 5, 136
Krolik, J. H., & Kallman, T. R. 1983, ApJ, 267, 610
Ku, W. H.-M., Righini-Cohen, G., & Simon, M. 1982, Science, 215, 61
Lada, E. A. 1992, ApJ, 393, L25
Lasker, B. N., Sturch, C. R., McLean, B. J., Russell, J. L., Jenkner, H., & Shara, M. M. 1990, AJ, 99, 2019
LaValley, M., Isobe, T., & Feigelson, E. D. 1992, BAAS, 24, 839
Leous, J. A., Feigelson, E. D., André, P., & Montmerle, T. 1991, ApJ, 379, 683
Levy, E. H., Ruzmaikin, A. A., & Ruzmaikina, T. V. 1991, in The Sun in Time, ed. C. P. Sonnett et al. (Tucson: Univ. Arizona Press), 589
Mangeney, A., & Praderie, F. 1984, A&A, 130, 143
Mattila, K., Liljeström, T., & Toriseva, M. 1989, in Low Mass Star Formation and Pre–Main-Sequence Objects, ed. B. Reipurth (Garching: ESO), 153
Mendenhall, J. A., & Burrows, D. N. 1993, in preparation
Micela, G., Sciortino, S., Vaiana, G. S., Harnden, F. R., Jr., Rosner, R., & Schmitt, J. H. 1990, ApJ, 348, 357
Micela, G., Sciortino, S., Vaiana, G. S., Schmitt, J. H., Stern, R. A., Harnden, F. R., Jr., & Rosner, R. 1988, ApJ, 325, 798
Montmerle, T., & André, P. 1989, in Low Mass Star Formation and Pre–Main-Sequence Objects, ed. B. Reipurth (Garching: ESO), 407
Montmerle, T., Feigelson, E. D., Bouvier, J., & André, P. 1993, in Protostars and Protoplanets III (Tucson: Univ. Arizona Press), 689
Montmerle, T., Koch-Miramond, L., Falgarone, E., & Grindlay, J. E. 1983, ApJ, 269, 182
Moshir, M., et al. 1992, Explanatory Supplement to the *IRAS* Faint Source Survey, Version 2, JPL D-10015 (Pasadena: JPL)
Mundt, R. 1981, A&A, 95, 234
Noyes, R. W., Hartmann, L. W., Baliunas, S. L., Duncan, D. K., & Vaughan, A. H. 1984, ApJ, 279, 763
Palla, F., & Stahler, S. W. 1993, preprint
Pallavicini, R., Golub, L., Rosner, R., Vaiana, G. S., Ayres, T., & Linsky, J. L. 1981, ApJ, 248, 279
Pepin, R. O. 1989, in The Formation and Evolution of Planetary Systems, ed. H. Weaver et al. (New York: Cambridge Univ. Press), 55
Prusti, T., Whittet, D. C., & Wesselius, P. R. 1992, MNRAS, 254, 361 (P92)
Röser, S., & Bastian, U. 1991, PPM Star Catalogue (Heidelberg: Spektrum Akad.)

Russell, J. L., Lasker, B. M., McLean, B. J., Sturch, C. J., & Jenkner, H. 1990, AJ, 99, 2059
Schmitt, J. H. 1985, ApJ, 293, 178
Schmitt, J. H., Golub, L., Harnden, F. R., Jr., Maxson, C. W., Rosner, R., & Vaiana, G. S. 1985, ApJ, 290, 307
Schmitt, J. H., Micela, G., Sciortino, S., Vaiana, G. S., Harnden, F. R., Jr., & Rosner, R. 1990, ApJ, 351, 492
Schwartz, R. D. 1977, ApJS, 35, 161
———. 1992, in Low Mass Star Formation in Southern Molecular Clouds, ed. B. Reipurth (Garching: ESO), 93 (S92)
Schwartz, R. D., & Henize, K. G. 1983, AJ, 88, 1665
Silk, J., & Norman, C. A. 1983, ApJ, 293, 542
Simon, T. 1992, in Cool Stars, Stellar Systems and the Sun, ed. M. S. Giampapa & S. A. Baliunas (San Francisco: ASP), 3
Skrutskie, M. F., Dutkevitch, D., Strom, S. E., Edwards, S., Strom, K. M., & Shure, M. A. 1990, AJ, 99, 1187
Skumanich, A. 1972, ApJ, 171, 565
Steenman, H., & Thé, R. S. 1989, Ap&SS, 161, 99
Stepień, K. 1988, ApJ, 335, 892
Stern, R. A., Schmitt, J. H., Rosso, C., Pye, J. P., Hodgkin, S. T., & Stauffer, J. R. 1992, ApJ, 399, L159
Stoy, R. H. 1968, Ann. Cape Obs., 22
Strom, K. M., Strom, S. E., Edwards, S., Cabrit, S., & Skrutskie, M. F. 1989, AJ, 97, 1451
Strom, K. M., et al. 1990, ApJ, 362, 168
Trümper, J. 1990, in High Resolution X-Ray Spectroscopy of Cosmic Plasmas, ed. P. Gorenstein & M. Zombeck (Cambridge: Cambridge Univ. Press), 291
Vandenberg, D. A., Hartwick, F. A., Dawson, P., & Alexander, D. R. 1983, ApJ, 266, 747
Walter, F. M. 1992, AJ, 104, 758 (W92)
Walter, F. M., & Barry, D. C. 1991, in The Sun in Time, ed. C. P. Sonnett et al. (Tucson: Univ. Arizona Press), 663
Walter, F. M., Brown, A., Mathieu, R. D., Myers, P. C., & Vrba, F. J. 1988, AJ, 96, 297
Walter, F. M., & Kuhi, L. V. 1981, ApJ, 250, 254
Whittet, D. C., Kirrane, T. M., Kilkenny, D., Oates, A. P., Watson, F. G., & King, D. J. 1987, MNRAS, 224, 497
Whittet, D. C., Prusti, T., & Wesselius, P. R. 1991, MNRAS, 249, 497
Zickgraf, F.-J., Humphreys, R. M., Graham, J. A., & Phillips, A. 1990, PASP, 102, 920